2014

Inversion of the Broken Ray Transform

Roman Krylov
University of Central Florida

STARS Citation

Krylov, Roman, "Inversion of the Broken Ray Transform" (2014). *Electronic Theses and Dissertations, 2004-2019*. 4610.
https://stars.library.ucf.edu/etd/4610

INVERSION OF THE BROKEN RAY TRANSFORM

by

ROMAN KRYLOV
B.S. Lomonosov Moscow State University, 2003
M.S. University of Central Florida, 2012

A dissertation submitted in partial fulfilment of the requirements
for the degree of Doctor of Philosophy
in the Department of Mathematics
in the College of Sciences
at the University of Central Florida
Orlando, Florida

Fall Term
2014

Major Professor: Alexander Katsevich

ABSTRACT

The broken ray transform (BRT) is an integral of a function along a union of two rays with a common vertex. Consider an X-ray beam scanning an object of interest. The ray undergoes attenuation and scatters in all directions inside the object. This phenomena may happen repeatedly until the photons either exit the object or are completely absorbed. In our work we assume the single scattering approximation when the intensity of the rays scattered more than once is negligibly small. Among all paths that the scattered rays travel inside the object we pick the one that is a union of two segments with one common scattering point. The intensity of the ray which traveled this path and exited the object can be measured by a collimated detector. The collimated detector is able to measure the intensity of X-rays from the selected direction. The logarithm of such a measurement is the broken ray transform of the attenuation coefficient plus the logarithm of the scattering coefficient at the scattering point (vertex) and a known function of the scattering angle.

In this work we consider the reconstruction of X-ray attenuation coefficient distribution in a plane from the measurements on two or three collimated detector arrays. We derive an exact local reconstruction formula for three flat collimated detectors or three curved or pin-hole collimated detectors. We obtain a range condition for the case of three curved or pin-hole detectors and provide a special case of the range condition for three flat detectors.

We generalize the reconstruction formula to four and more detectors and find an optimal set of parameters that minimize noise in the reconstruction. We introduce a more accurate scattering model which takes into account energy shifts due to the Compton effect, derive an exact reconstruction formula and develop an iterative reconstruction method for the energy-dependent case. To solve the problem we assume that the radiation source is monoenergetic and the dependence of the attenuation coefficient on energy is linear on an energy interval from the minimal to the maximal

scattered energy. We find the parameters of the linear dependence of the attenuation on energy as a function of a point in the reconstruction plane.

ACKNOWLEDGMENTS

This research was supported in part by NSF grants DMS-0806304 and DMS-1115615

TABLE OF CONTENTS

LIST OF FIGURES

LIST OF TABLES

CHAPTER 1: LITERATURE REVIEW

The books [Bus02], [Pod10] are comprehensive references on the physics of medical imaging that describe in details the Compton scattering and absorption phenomena used in our work.

Reconstruction of a function f knowing its integrals along all lines (i.e., the Radon transform of f) is a classical and well-investigated subject (see e.g. [Nat01]). The line integrals can be found by transmitting narrow x-ray beams through an object and measuring the intensity of the outgoing radiation. The main physical assumption that allows the recovery of line integrals from such data is that scattering is neglected. Taking scattering into consideration by assuming the single-scattering approximation is a promising idea, which has recently attracted renewed interest (see e.g. [FSM09, MNTZ10, FMS11, TN11, Amb12] and references therein). Applications of this idea to imaging range from optics [FSM09] to Compton scattering [BZG97, MNTZ10, TN11]. The corresponding mathematical model is the Broken-Ray transform (BRT) (also known as the V-line transform). As opposed to the classical line transform, here we assume that we know the integrals of f along a family of broken rays. Each broken ray is the union of two rays having a common vertex. The family of broken rays and the corresponding integration weight depend on the specific physical model.

The following selected publications study the inverse problem of the BRT arising in various contexts from optics to medical radiology.

The paper [FSM09] presents algebraic iterative reconstruction of the attenuation coefficient from the measured scattering data assuming single scattering approximation. The authors show that the inverse problem of BRT does not result in additional ill posedness comparing to the inversion of the classical Radon Transform in two dimensions.

The paper [MNTZ10] studies the application of the BRT to the emission tomography. The V-Line transform, formulated as a two-dimensional version of the Conical Radon Transform, is defined similarly to the Broken Ray Transform. The difference is that the integrand in the V-Line transform is inversely proportional to the distance from the emission point. The authors provide two mathematically equivalent methods of reconstruction. First reconstruction method uses Fourier transform. Second method derives the adjoint operator and builds the reconstruction formula with the filtered back-projection structure.

The paper [FMS11] studies the properties of the BRT in the context of single-scattering optical tomography (SSOT). One inversion formula provided is for the spatially uniform scattering case, when the scattering coefficient is constant inside the object. Another, more general inversion formula follows for the case of non-uniform scattering.

The most recent work in the area [ZSM14] investigates reconstruction of the Star Transform — a generalization of the Broken Ray Transform defined as a linear combination of BRTs. The authors consider various ways of reconstruction of the Star Transform, one of which, in addition to scattered rays, can automatically take into account the ballistic (non-scattered) rays for better reconstruction stability. The reconstruction method given by (12) in [ZSM14] is equivalent to our reconstruction formula (3.11) that was first published in [KK13]. In our work we make some advances beyond [ZSM14] by handling energy-dependent attenuation and finding the formula that minimizes noise in the reconstructed images.

Works [GKKW73, CD73, Bra83, HK87, CW11] study the physical aspects and reconstruction methods of the scattering and attenuation coefficients from scattered rays.

The work [Bra83] studies X-rays back-scattering for reconstruction of the attenuation and scattering coefficients. Author states how challenging the problem of scattering tomography is:

> Although the system described is not medically useful because of patient dose constraints and the insensitivity of the method to small density changes, it is believed that the system described has industrial applications.

A noteworthy method described in the work is the original way to directly reconstruct the scattering coefficient:

> Attenuation of the emerging scatter signal by overlying tissues was found to be a significant problem, and Garnett et al. and Clarke and Van Dyk individually proposed a two-source method for determining electron density which would be independent of such attenuation ([GKKW73],[CD73]). In the two-source method two sources of different energies are used, where the energy of the second source corresponds to the Compton-scattered energy of the first source for the scattering angle of interest. Measurements are made of the scattered and transmitted beams for two patient orientstions, at the initial position and then after a $180°$ rotation, and the electron density in a scattering volume can then be found, independent of overlying tissues.

Paper [HK87] studies classical coherent (Thomson) x-ray scattering imaging for reconstruction of the scattering coefficient.

The authors use classical filtered back-projection method to reconstruct the attenuation using the measurements from the ballistic rays. Then using measurements on the offset detectors they reconstruct the scattering coefficient distribution. The authors rely on the measurements with the direction and energy sensitive detectors. This data acquisition method is an alternative to the collimated detector arrays

Paper [CW11] studies iterative reconstruction of attenuation and scattering coefficients in soft biological tissues.

Our work [KK13] is the first one providing the local inversion formula of BRT for the case of three detectors which involves only first derivatives of the measured data. This yields a simple and stable numerical reconstruction algorithm. The work [ZSM14] provides an equivalent reconstruction formula for the Star Transform — a generalization of the BRT for the case of three or more detectors. In our current work we continue to study various approaches to inverting the BRT in a more accurate model taking into account Compton energy shifts and allowing for the optimization with respect to noise stability. To accommodate multiple scattering energies we use linear approximation of the dependence of the attenuation coefficient on energy.

CHAPTER 2: THE CASE OF THREE DETECTORS

2.1 Introduction.

Similarly to [FSM09, FMS11], we consider an experiment in which a narrow x-ray beam is incident on an object. The support of the object is the closure of an open convex set U with a piecewise-smooth boundary. The latter is denoted ∂U. The outgoing radiation is detected by two or more collimated detectors D_i (see Fig. 2.1). Thus, for each $x \in U$ and each D_i there is a unique direction $\beta_i(x)$ such that the x-rays propagating along the ray

$$R_i(x) := \{y \in \mathbb{R}^2 : \ y = x + t\beta_i(x), t \geq 0\} \tag{2.1}$$

are detected by the appropriate bin on D_i. Let μ_s and μ_a be the scattering and absorption coefficients of the object, respectively. Denote $\mu_{tot} = \mu_s + \mu_a$. Let α be the unit vector defining the direction of the incident beam. Under the single scattering approximation the data collected by the ith detector are proportional to the expression

$$KN(\alpha, \beta_i)\mu_s(x) \exp\left\{-\int_0^\infty \mu_{tot}(x - t\alpha)dt - \int_{R_i(x)} \mu_{tot} dt\right\}. \tag{2.2}$$

Here $KN(\alpha, \beta_i)$ is the Klein-Nishina function which gives the probability of scattering along any given direction. Note that this function is known and independent of the medium.

For simplicity, our model assumes that the energy loss of the photons due to scattering is negligible. This assumption holds if the incident photons are of relatively low energy. Otherwise, we would have to consider two μ_{tot}: before the scattering event and after. If the detectors are positioned fairly symmetrically with respect to the incident beam, the scattered photons will have approximately the same energy and the requirement that incident photons have low energy can be relaxed. Since the proposed algorithm uses the differences between detector data, we will reconstruct μ_{tot}, which corresponds to the energy of the scattered photons. Our model neglects also the effect of the binding energy correction (assuming, in particular, that forward scattered photons are not detected), see [Pod10], pp. 322-325.

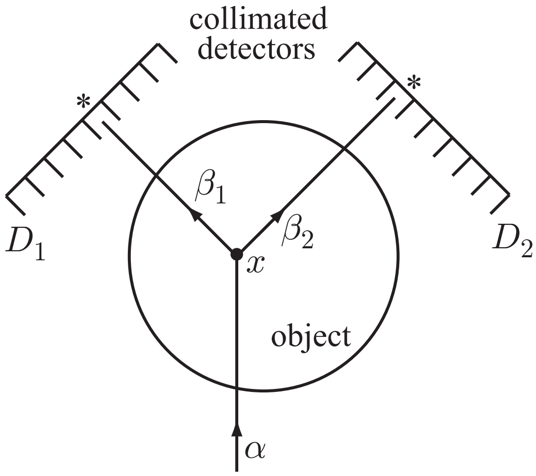

Figure 2.1: Illustration of BRT-based imaging.

Assuming that $\mu_s(x) > 0$, taking the logarithm of equation (2.2) written for each detector, subtracting the two resulting equations, and accounting for the known factors (e.g., the Klein-Nishina function) yields the Broken Ray Transform (BRT)

$$g_{ij}(x) = \int_{R_i(x)} \mu_{tot} dt - \int_{R_j(x)} \mu_{tot} dt \tag{2.3}$$

for any pair of detectors D_i, D_j. By moving the incident beam, say, from left to right parallel to α, and by utilizing different pairs of detector bins, we can get $g_{ij}(x)$ for all x in the support of the object (i.e. where $\mu_s(x) > 0$). To simplify the notation, in what follows we denote $f(x) := \mu_{tot}(x)$. Let ∇_i denote the directional derivative along β_i.

Similarly to [FSM09, FMS11], we suppose at the beginning that we have two detectors and they are flat. In this case $\beta_i(x), i = 1, 2$, are constants. Applying $\nabla_1\nabla_2$ we get a first order constant coefficient partial differential equation for f, which can be solved by the method of characteristics. See [FMS11], where an alternative inversion formula was first derived. In this work we study several new problems related to the BRT. In particular, we consider more general, curved detectors that are focused at a fixed point. In other words, for each detector D_i there exists a fixed point $x_0^{(i)}$ (the focus of D_i) such that all rays detected by D_i belong to lines passing through $x_0^{(i)}$. If D_i is concave relative to U, the vectors $\beta_i(x)$ point away from $x_0^{(i)}$. If D_i is convex, the vectors $\beta_i(x)$ point towards $x_0^{(i)}$ (see Fig. 2.2). Note that such detectors are common in medical imaging. In conventional CT the detectors are typically concave, and pin-hole cameras in nuclear imaging correspond to convex detectors. In what follows we allow the detectors to be flat. In this case the corresponding focus $x_0^{(i)}$ is the point at infinity and $\beta_i(x)$ is the same for all x.

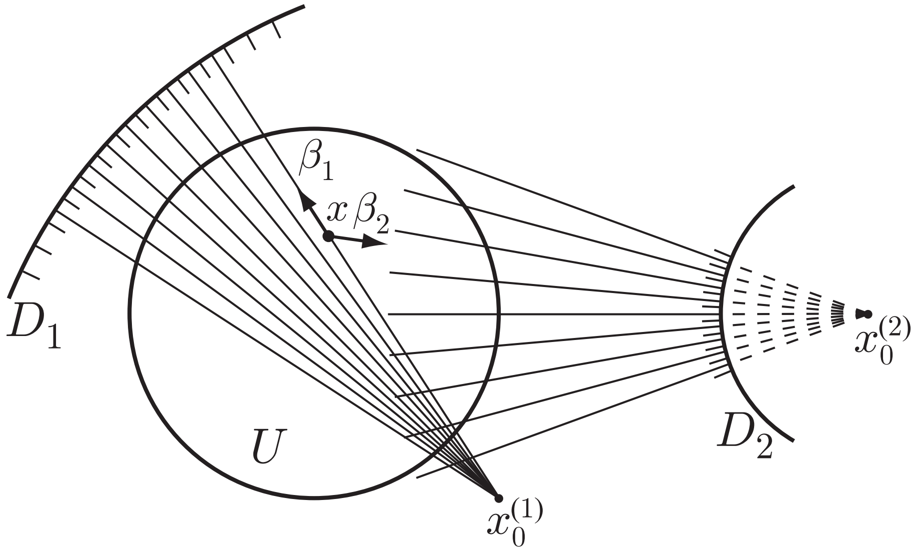

Figure 2.2: Illustration of concave (D_1) and convex (D_2) detectors.

It is clear that in order to invert the BRT, we would like to have as much data as possible. On the other hand, from the description of the experiment it is reasonable to assume that we know the BRT only for x where $f(x) > 0$. In section 2.2 our assumptions are that supp $f = \overline{U}$ (the closure of U), $f \in C_0^2(U)$, and we know $g_{12}(x)$ for all $x \in U$. We obtain a first order partial differential equation for f with non-constant coefficients. Similarly to the flat case, the equation can be solved by the method of characteristics. Using that $f = 0$ on the boundary of U allows us to integrate along the characteristics and recover f. From the practical standpoint, the disadvantages of this inversion algorithm are that it requires computation a second order derivative of the data and integration along characteristics.

In section 2.3 we relax the assumption on f and assume that $f \in C^2(\overline{U})$. Thus f need not go to zero at the boundary of U. Only in this section the two detectors are flat. In addition to the BRT (2.3), in this section we also consider another version of the BRT that was studied in [FSM09, FMS11]. In this version there is a plus between the integrals in (2.3) instead of a minus. Using the approach based on characteristics, we obtain inversion algorithms for both BRTs that work for any convex U. In the case of the BRT with a minus we show that there may be a subset of U where f could not be determined in principle. The inversion formulas of [FMS11] for both BRTs were derived in the case when U is a rectangular slab and were based on a Fourier transform approach.

As was mentioned above, inversion of the BRT in the case of two detectors has some practical disadvantages. In section 2.4 we assume $f \in C^1(\overline{U})$ and consider the case of three detectors. It turns out that having an extra detector allows us to come up with an inversion formula that involves only the first order derivatives of the data. Moreover, the formula is purely local, i.e. it does not involve any integration and solves the so-called interior problem. Regardless of whether there are two detectors or three, neither the object nor the source and detectors require a rotation in order to obtain a complete data set.

In section 2.5 we obtain a range condition and formulate a range theorem for the BRT in the case of three detectors. For the purposes of the theorem, we assume that the data are given for all $x \in \mathbb{R}^2$, even though $f \in C_0^\infty(U)$. If the data are not given for all x, our results provide a necessary condition on the range.

Finally, some numerical experiments are presented in section 2.6.

2.2 The two-detector case

In this section we derive a first order linear partial differential equation from which f may be found. As follows from (2.3), our data are

$$g_{ij}(x) = \int_0^\infty f(x + t\beta_i(x))dt - \int_0^\infty f(x + t\beta_j(x))dt,\ i, j = 1, 2,\ i \neq j,\ x \in U, \tag{2.4}$$

and we assume $f \in C_0^2(U)$. Clearly,

$$\nabla_i = c_{ij}\nabla_j + c_{ij}^\perp \nabla_j^\perp, \tag{2.5}$$

where

$$c_{ij} := \beta_i \cdot \beta_j,\ c_{ij}^\perp := \beta_i \cdot \beta_j^\perp. \tag{2.6}$$

Here $\nabla_j^\perp := \nabla_{\beta_j^\perp}$, and $\beta_j^\perp$ is the unit vector obtained from β_j by rotating it 90° counterclockwise. For simplicity, here and in what follows the dependence of $c_{ij}, c_{ij}^\perp, \beta_i, \beta_i^\perp$ on x is omitted from notation. In the case when ∇_i is applied to a vector field, it is realized as the usual directional derivative on scalar functions applied to each component of the given vector. From the description of the experiment it is clear that we can assume

$$\nabla_i \beta_i(x) = 0 \tag{2.7}$$

for all i. Since $|\beta_i(x)| \equiv 1$, we define $l_i(x)$ from the equation

$$\nabla_i^\perp \beta_i(x) = -l_i(x)\beta_i^\perp(x). \tag{2.8}$$

If the detector D_i is flat, we take $l_i(x) \equiv 0$. If the detector is concave relative to U, then $l_j(x) = -|x - x_0^{(j)}|^{-1}$ (see Fig. 2.2, detector D_1). If the detector is convex, then $l_j(x) = |x - x_0^{(j)}|^{-1}$ (see Fig. 2.2, detector D_2). By direct calculation we obtain the following useful identity:

$$\nabla_j \nabla_j^\perp - \nabla_j^\perp \nabla_j = l_j(x)\nabla_j^\perp. \tag{2.9}$$

Using (2.4) – (2.7) we obtain:

$$\begin{aligned} \nabla_i g_{ij}(x) =& - f(x) + c_{ij} f(x) - c_{ij}^\perp \nabla_j^\perp \int_0^\infty f(x + t\beta_j)dt \\ =& (-1 + c_{ij}) f(x) - c_{ij}^\perp J_j(x), \end{aligned} \tag{2.10}$$

where we have defined

$$J_j(x) := \nabla_j^\perp \int_0^\infty f(x + t\beta_j)dt. \tag{2.11}$$

Using (2.5), (2.7) and (2.8) gives

$$\begin{aligned} \nabla_j c_{ij} =& [\nabla_j \beta_i] \cdot \beta_j = [(c_{ji}\nabla_i + c_{ji}^\perp \nabla_i^\perp)\beta_i] \cdot \beta_j \\ =& - c_{ji}^\perp l_i(x) c_{ji}^\perp = -l_i(x)(c_{ji}^\perp)^2, \end{aligned} \tag{2.12}$$

$$\nabla_j c_{ij}^\perp = [\nabla_j \beta_i] \cdot \beta_j^\perp = -c_{ji}^\perp l_i(x) \beta_i^\perp \cdot \beta_j^\perp = -l_i(x) c_{ji}^\perp c_{ij}. \tag{2.13}$$

Applying ∇_j to (2.10) gives

$$\begin{aligned}\nabla_j \nabla_i g_{ij}(x) =& - l_i(x)(c_{ji}^{\perp})^2 f(x) + (-1 + c_{ij})\nabla_j f(x) \\ &+ l_i(x) c_{ji}^{\perp} c_{ij} J_j(x) - c_{ij}^{\perp} \nabla_j J_j(x).\end{aligned} \tag{2.14}$$

Consider the last term in (2.14). Using (2.9) and (2.11) we find

$$\nabla_j J_j(x) = (\nabla_j^{\perp} \nabla_j + l_j(x)\nabla_j^{\perp}) \int_0^{\infty} f(x + t\beta_j) dt = -\nabla_j^{\perp} f(x) + l_j(x) J_j(x). \tag{2.15}$$

Using (2.15), solving (2.10) for J_j, and substituting into (2.14) gives

$$\begin{aligned}\nabla_j \nabla_i g_{ij}(x) =& - l_i(x)(c_{ji}^{\perp})^2 f(x) + (-1 + c_{ij})\nabla_j f(x) + c_{ij}^{\perp} \nabla_j^{\perp} f(x) \\ &+ (l_i(x) c_{ji}^{\perp} c_{ij} - c_{ij}^{\perp} l_j(x)) \frac{(-1 + c_{ij}) f(x) - \nabla_i g_{ij}(x)}{c_{ij}^{\perp}}.\end{aligned} \tag{2.16}$$

After some simplifications we get a first-order partial differential equation:

$$\begin{aligned}&(l_j(x) - l_i(x))(1 - c_{ij}) f(x) + (\nabla_i - \nabla_j) f(x) \\ &\quad = \nabla_j \nabla_i g_{ij}(x) - (l_i(x) c_{ij} + l_j(x)) \nabla_i g_{ij}(x).\end{aligned} \tag{2.17}$$

As in the case of flat detectors, equation (2.17) can be solved for f by the method of characteristics. Note that the characteristics are ellipses with foci $x_0^{(1)}$ and $x_0^{(2)}$ if none of the detectors is flat. The easiest way to see this is by using the well-known reflection property of ellipses. Indeed, let Γ be an ellipse with foci $x_0^{(1)}$ and $x_0^{(2)}$. Pick any $x \in \Gamma$. From the reflection property, $\beta_1(x) - \beta_2(x)$ is tangent to Γ at x, so $\nabla_1 - \nabla_2$ differentiates along the direction tangent to Γ. Since $x \in \Gamma$ is arbitrary, the desired assertion follows. If one of the detectors, say D_1, is flat, then the characteristics are parabolas with the focus $x_0^{(2)}$ and axis $R_1(x_0^{(2)})$. This fact can be established from the reflection property of parabolas. If both D_1 and D_2 are flat, the characteristics are parallel lines. As initial conditions, we can use that $f \equiv 0$ on ∂U.

2.3 The case when f is discontinuous across the boundary of U

Suppose that $f \in C^2(\overline{U})$. In this section only we also assume that both detectors are flat. Setting $i = 1$, $j = 2$ and $l_1 = l_2 = 0$ in (2.17) we get

$$(\nabla_1 - \nabla_2) f(x) = \nabla_2 \nabla_1 g_{12}(x). \tag{2.18}$$

In order to find f by integrating along the characteristics of (2.18) we need to know f on a non-characteristic curve inside U. Equation (2.18) does not provide this information, because the equation was derived by differentiating the data two times and some information got lost. In this section we show how to find f on a line segment inside U. This is done using both the first and second derivatives of the data.

Choose the x_1-axis along the characteristic direction and suppose

$$\beta_1 = (\cos\gamma, \sin\gamma),\ \beta_2 = (-\cos\gamma, \sin\gamma). \tag{2.19}$$

Note that $\cos\gamma \neq 0$, since we assume that β_1 and β_2 are not parallel. Then

$$2\cos\gamma \frac{\partial}{\partial x_1} = \nabla_1 - \nabla_2. \tag{2.20}$$

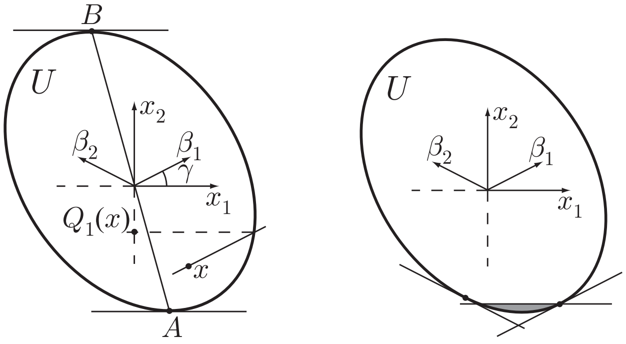

Figure 2.3: Illustration of the inversion algorithm in the case $f \in C^1(\overline{U})$.

Denote

$$x_2^{\text{inf}} := \inf_{x\in U} x_2,\ x_2^{\text{sup}} := \sup_{x\in U} x_2, \tag{2.21}$$

and let $A, B \in \overline{U}$ be two points with x_2-coordinates equal to x_2^{inf} and x_2^{sup}, respectively (see Fig. 2.3, left panel). Note that these points need not be unique. Integrating (2.18) and using (2.20) we find

$$f(x) = f(x_1(x_2), x_2) + \frac{1}{2\cos\gamma}\int_{x_1(x_2)}^{x_1} \nabla_2\nabla_1 g_{12}(s, x_2)ds, \tag{2.22}$$

where $x_1 = x_1(x_2)$ is the equation of the line segment AB. Clearly, if we know f on the segment AB, then we can find f everywhere inside U using (2.22). Denote

$$\phi(x_2) := f(x_1(x_2), x_2), \tag{2.23}$$

Then (2.4) can be rewritten as follows:

$$g_{12}(x) = \int_0^{T_1(x)} \phi(x_2 + t\sin\gamma)dt - \int_0^{T_2(x)} \phi(x_2 + t\sin\gamma)dt + G(x), \tag{2.24}$$

where $T_j(x), j = 1, 2,$ is the value of t such that the ray $R_j(x)$ intersects ∂U, and $G(x)$ is a function computable from the data (i.e. from g_{12}) by way of (2.22). Changing variables, transform (2.24) as follows:

$$\begin{aligned} g_{12}(x) &= \frac{1}{\sin\gamma}\left(\int_{x_2}^{Q_1(x)} \phi(s)ds - \int_{x_2}^{Q_2(x)} \phi(s)ds\right) + G(x) \\ &= \frac{1}{\sin\gamma}\int_{Q_2(x)}^{Q_1(x)} \phi(s)ds + G(x). \end{aligned} \tag{2.25}$$

Here $Q_j(x)$ is the x_2-coordinate of the point of intersection of the ray $R_j(x)$ and ∂U. See Fig. 2.3, where the construction of $Q_1(x)$ is illustrated. Clearly,

$$\nabla_j Q_j(x) = 0,\ j = 1, 2, \tag{2.26}$$

so (2.25) implies

$$\begin{aligned} \nabla_1(g_{12}(x) - G(x)) &= -\frac{\nabla_1 Q_2(x)}{\sin\gamma}\phi(Q_2(x)), \\ \nabla_2(g_{12}(x) - G(x)) &= \frac{\nabla_2 Q_1(x)}{\sin\gamma}\phi(Q_1(x)). \end{aligned} \tag{2.27}$$

By construction,

$$c_{12} = -\cos(2\gamma),\ c_{12}^{\perp} = \sin(2\gamma). \tag{2.28}$$

Using (2.5), (2.26) and (2.28) gives

$$\begin{aligned} \nabla_1 Q_2(x) &= c_{12}^{\perp}\nabla_2^{\perp} Q_2(x) = \sin(2\gamma)\nabla_2^{\perp} Q_2(x), \\ \nabla_2 Q_1(x) &= -c_{12}^{\perp}\nabla_1^{\perp} Q_1(x) = -\sin(2\gamma)\nabla_1^{\perp} Q_1(x). \end{aligned} \tag{2.29}$$

Hence (2.29) becomes

$$\phi(Q_j(x)) = \frac{\nabla_i(g_{12}(x) - G(x))}{-2\cos\gamma[\nabla_j^{\perp} Q_j(x)]},\ i = 1, j = 2 \text{ or } i = 2, j = 1. \tag{2.30}$$

We assumed that U is convex, hence $\nabla_j^\perp Q_j(x) \neq 0$ for all $x \in U$ such that $Q_j(x) < x_2^{\text{sup}}$. Equations (2.25) and (2.30) show that $\phi(x_2)$ can be recovered only inside the interval

$$x_2 \in (\inf_{x\in U} \min\{Q_1(x), Q_2(x)\}, \sup_{x\in U} \max\{Q_1(x), Q_2(x)\}). \tag{2.31}$$

If $0 < \gamma < \pi/2$, then $x_2 < \min\{Q_1(x), Q_2(x)\}$, so

$$x_2^{\text{inf}} \leq \inf_{x\in U} \min\{Q_1(x), Q_2(x)\}, \quad x_2^{\text{sup}} = \sup_{x\in U} \max\{Q_1(x), Q_2(x)\}. \tag{2.32}$$

In other words, there may be a 'shadow' zone near the bottom of U where $\phi(x_2)$ cannot be determined (see Fig. 2.3, right panel). Similarly, if $-\pi/2 < \gamma < 0$, then $x_2 > \max\{Q_1(x), Q_2(x)\}$ and

$$x_2^{\text{inf}} = \inf_{x\in U} \min\{Q_1(x), Q_2(x)\}, \quad x_2^{\text{sup}} \geq \sup_{x\in U} \max\{Q_1(x), Q_2(x)\}, \tag{2.33}$$

i.e. the shadow zone may now be near the top of U. If $\gamma = 0$, i.e. the two detectors are opposite each other, then (2.18) implies that all of f inside U can be determined by an obvious formula:

$$f(x) = -\frac{1}{2}\nabla_1 g_{12}(x), \; x \in U. \tag{2.34}$$

Using the same approach, we can obtain an inversion algorithm for another BRT considered in [FSM09, FMS11]:

$$\tilde{g}_{12}(x) := \int_0^\infty f(x + t\beta_1(x))dt + \int_0^\infty f(x + t\beta_2(x))dt, \; x \in U. \tag{2.35}$$

In [FSM09, FMS11] the set U is an infinite strip. Here, as in the rest of the work, we assume that

U is an open convex set with a piecewise smooth boundary. Similarly to (2.18),

$$(\nabla_1 + \nabla_2) f(x) = \nabla_2 \nabla_1 \tilde{g}_{12}(x). \tag{2.36}$$

We introduce the coordinate system such that (2.19) holds and the characteristics of (2.36) are parallel to the x_2-axis. Thus,

$$2 \sin \gamma \frac{\partial}{\partial x_2} = \nabla_1 + \nabla_2. \tag{2.37}$$

Denote

$$x_1^{\text{inf}} := \inf_{x \in U} x_1, \; x_1^{\text{sup}} := \sup_{x \in U} x_1, \tag{2.38}$$

and let $A, B \in \overline{U}$ be two points with x_1-coordinates equal to x_1^{inf} and x_1^{sup}, respectively. Let $x_2 = x_2(x_1)$ be the equation of the line segment AB. As before, appealing to the method of characteristics, finding f in U reduces to finding f on AB. Denote also

$$\phi(x_1) := f(x_1, x_2(x_1)). \tag{2.39}$$

Similarly to (2.22),

$$f(x_1, x_2) = \phi(x_1) + \frac{1}{2 \sin \gamma} \int_{x_2(x_1)}^{x_2} \nabla_2 \nabla_1 \tilde{g}_{12}(x_1, s) ds. \tag{2.40}$$

Hence

$$\begin{aligned} \tilde{g}_{12}(x) &= \int_0^{T_1(x)} \phi(x_1 + t \cos \gamma) dt + \int_0^{T_2(x)} \phi(x_1 - t \cos \gamma) dt + \tilde{G}(x) \\ &= \frac{1}{\cos \gamma} \left(\int_{x_1}^{S_1(x)} \phi(s) ds + \int_{S_2(x)}^{x_1} \phi(s) ds \right) + \tilde{G}(x) \\ &= \frac{1}{\cos \gamma} \int_{S_2(x)}^{S_1(x)} \phi(s) ds + \tilde{G}(x), \end{aligned} \tag{2.41}$$

where $\tilde{G}(x)$ is a function computable from the data, T_j's are the same as before, $S_j(x)$ is the x_1-coordinate of the point of intersection of the ray $R_j(x)$ and ∂U, and we have used (2.19). Differentiation gives

$$\begin{aligned}\nabla_1(\tilde{g}_{12}(x) - \tilde{G}_1(x)) &= -\frac{\nabla_1 S_2(x)}{\cos\gamma}\phi(S_2(x)),\\ \nabla_2(\tilde{g}_{12}(x) - \tilde{G}_2(x)) &= \frac{\nabla_2 S_1(x)}{\cos\gamma}\phi(S_1(x)),\end{aligned} \tag{2.42}$$

and it is easy to see that the coefficients in (2.42) are finite and not equal zero. Moreover, since U is convex, for any $x_1 \in (x_1^{\text{inf}}, x_1^{\text{sup}})$ there is a point $x \in U$ such that either $x_1 = S_1(x)$ or $x_1 = S_2(x)$. This proves that $f(x)$ can be computed for all $x \in U$. Since the proof is constructive, this also gives an algorithm for computing f.

Strictly speaking, since ∂U is piecewise smooth, the derivatives on the right in (2.30) may not exist for those x and j such that the ray $R_j(x)$ passes through a point where ∂U is not smooth. On the other hand, $\phi(Q_j(x))$ is continuous. Hence at these exceptional points the right-hand side of (2.30) can be understood as a one-sided limit. The same argument applies to (2.42).

2.4 Three detectors

Suppose now we have three detectors $D_j, j = 1, 2, 3$. In this section we assume that $f \in C^1(U)$. Applying (2.10) twice we get

$$\begin{aligned}\nabla_1 g_{12}(x) =&(-1 + c_{12})f(x) - c_{12}^{\perp} J_2(x),\\ \nabla_3 g_{32}(x) =&(-1 + c_{32})f(x) - c_{32}^{\perp} J_2(x).\end{aligned} \tag{2.43}$$

Solving (2.43) for f after some transformations leads to an inversion formula:

$$f(x) = -\frac{c_{32}^{\perp}\nabla_1 g_{12}(x) + c_{21}^{\perp}\nabla_3 g_{32}(x)}{c_{32}^{\perp} + c_{21}^{\perp} + c_{13}^{\perp}}. \tag{2.44}$$

Similarly to section 2.3, at the points where $R_2(x)$ contains a point where ∂U is not smooth, the corresponding derivative $\nabla_j g_{j2}$, $j = 1$ or 2, is understood as a one-sided limit. Using the following identity, which can be checked by direct verification,

$$c_{32}^{\perp}\nabla_1 + c_{21}^{\perp}\nabla_3 + c_{13}^{\perp}\nabla_2 \equiv 0, \tag{2.45}$$

we can write (2.44) in a more symmetric form

$$f(x) = -\frac{c_{32}^{\perp}\nabla_1 g_1(x) + c_{21}^{\perp}\nabla_3 g_3(x) + c_{13}^{\perp}\nabla_2 g_2(x)}{c_{32}^{\perp} + c_{21}^{\perp} + c_{13}^{\perp}}. \tag{2.46}$$

2.5 A range condition

In this section we assume that $f \in C_0^{\infty}(U)$ and the data are given for all $x \in \mathbb{R}^2$. Our goal is to describe the range of the BRT. We start with deriving a necessary condition. Then we state a theorem, which provides the desired range characterization.

It is convenient to denote

$$\Sigma := c_{32}^{\perp} + c_{21}^{\perp} + c_{13}^{\perp}. \tag{2.47}$$

Similarly to (2.12) we get the following useful relations:

$$\begin{aligned}
&\nabla_i\beta_i = 0, && \nabla_i^\perp\beta_i = -l_i\beta_i^\perp,\\
&\nabla_i\beta_j = -c_{ij}^\perp l_j\beta_j^\perp, && \nabla_i^\perp\beta_j = -c_{ij}l_j\beta_j^\perp,\\
&\nabla_i\beta_i^\perp = 0, && \nabla_i^\perp\beta_i^\perp = l_i\beta_i,\\
&\nabla_i\beta_j^\perp = c_{ij}^\perp l_j\beta_j, && \nabla_i^\perp\beta_j^\perp = c_{ij}l_j\beta_j,\ i,j=1,2,3,\ i\neq j.
\end{aligned} \tag{2.48}$$

Some of these relations have already been used before, but they are collected here for convenience. Solving (2.43) for J_2 we get

$$J_2(x) = \frac{(1-c_{32})\nabla_1 g_{12}(x) - (1-c_{12})\nabla_3 g_{32}(x)}{\Sigma}. \tag{2.49}$$

Applying ∇_2 on both sides of (2.49) and using (2.15) with $j=2$ we find

$$-\nabla_2^\perp f(x) + l_2(x)J_2(x) = \nabla_2\frac{(1-c_{32})\nabla_1 g_{12}(x) - (1-c_{12})\nabla_3 g_{32}(x)}{\Sigma}. \tag{2.50}$$

Using (2.44) and (2.49) in (2.50) leads to a range condition

$$\begin{aligned}
\nabla_2^\perp\frac{c_{32}^\perp\nabla_1 g_{12}(x) + c_{21}^\perp\nabla_3 g_{32}(x)}{\Sigma} &+ l_2(x)\frac{(1-c_{32})\nabla_1 g_{12}(x) - (1-c_{12})\nabla_3 g_{32}(x)}{\Sigma}\\
&= \nabla_2\frac{(1-c_{32})\nabla_1 g_{12}(x) - (1-c_{12})\nabla_3 g_{32}(x)}{\Sigma}.
\end{aligned} \tag{2.51}$$

Denoting $\phi_1 := \nabla_1 g_{12}$ and $\phi_3 := \nabla_3 g_{32}$, rewrite (2.51) as follows:

$$\begin{aligned}
&\left\{\nabla_2^\perp\frac{c_{32}^\perp\phi_1(x)}{\Sigma} + l_2(x)\frac{(1-c_{32})\phi_1(x)}{\Sigma} - \nabla_2\frac{(1-c_{32})\phi_1(x)}{\Sigma}\right\}\\
&+\left\{\nabla_2^\perp\frac{c_{21}^\perp\phi_3(x)}{\Sigma} - l_2(x)\frac{(1-c_{12})\phi_3(x)}{\Sigma} + \nabla_2\frac{(1-c_{12})\phi_3(x)}{\Sigma}\right\} = 0.
\end{aligned} \tag{2.52}$$

After some manipulations, we can rewrite (2.52) in the form

$$\frac{(\nabla_3-\nabla_2)\phi_1+(\nabla_2-\nabla_1)\phi_3}{\Sigma}+\frac{A_1\phi_1+A_3\phi_3}{\Sigma^2}=0, \tag{2.53}$$

where

$$\begin{aligned} A_1&=\Sigma^2\left[\nabla_2^{\perp}\left(\frac{c_{32}^{\perp}}{\Sigma}\right)+l_2(x)\frac{1-c_{32}}{\Sigma}-\nabla_2\left(\frac{1-c_{32}}{\Sigma}\right)\right],\\ A_3&=\Sigma^2\left[\nabla_2^{\perp}\left(\frac{c_{21}^{\perp}}{\Sigma}\right)-l_2(x)\frac{1-c_{12}}{\Sigma}+\nabla_2\left(\frac{1-c_{12}}{\Sigma}\right)\right]. \end{aligned} \tag{2.54}$$

Using (2.48), we obtain after lengthy calculations:

$$\begin{aligned} A_1&=(c_{12}-c_{13})(c_{13}^{\perp}+c_{21}^{\perp})l_1+(1-c_{23})(c_{21}^{\perp}+c_{32}^{\perp})l_2+(c_{23}-1)(c_{13}^{\perp}+c_{32}^{\perp})l_3,\\ A_3&=(1-c_{12})(c_{13}^{\perp}+c_{21}^{\perp})l_1+(c_{12}-1)(c_{21}^{\perp}+c_{32}^{\perp})l_2+(c_{13}-c_{23})(c_{13}^{\perp}+c_{32}^{\perp})l_3. \end{aligned} \tag{2.55}$$

In addition, with the help of (2.9) we find that

$$\nabla_i\nabla_j-\nabla_j\nabla_i=-c_{ij}^{\perp}(l_i\nabla_i^{\perp}+l_j\nabla_j^{\perp}). \tag{2.56}$$

Using (2.55), (2.56), and the identity

$$\begin{aligned} &-(\nabla_3-\nabla_2)\nabla_1-(\nabla_2-\nabla_1)\nabla_3\\ &\quad=(\nabla_1-\nabla_3)\nabla_2+[(\nabla_1\nabla_3-\nabla_3\nabla_1)+(\nabla_2\nabla_1-\nabla_1\nabla_2)+(\nabla_3\nabla_2-\nabla_2\nabla_3)], \end{aligned} \tag{2.57}$$

we can rewrite (2.53) in a more symmetric way (see appendix   for additional details):

$$\begin{aligned} &(\nabla_3-\nabla_2)\nabla_1 g_1+(\nabla_1-\nabla_3)\nabla_2 g_2+(\nabla_2-\nabla_1)\nabla_3 g_3\\ &\qquad+\frac{A_1\nabla_1 g_1+A_2\nabla_2 g_2+A_3\nabla_2 g_2}{\Sigma}=0, \end{aligned} \tag{2.58}$$

where

$$A_2 = (c_{13} - 1)(c_{13}^{\perp} + c_{21}^{\perp})l_1 + (c_{23} - c_{12})(c_{21}^{\perp} + c_{32}^{\perp})l_2 + (1 - c_{13})(c_{13}^{\perp} + c_{32}^{\perp})l_3, \tag{2.59}$$

and $g_j, j = 1, 2, 3$, are any three C^1 functions such that $g_{ij} = g_i - g_j$ for all pairs i, j. Let us note that if all the detectors are flat, i.e. $l_i = 0$ for all i, then the range condition simplifies as follows:

$$(\nabla_3 - \nabla_2)\nabla_1 g_1 + (\nabla_1 - \nabla_3)\nabla_2 g_2 + (\nabla_2 - \nabla_1)\nabla_3 g_3 = 0. \tag{2.60}$$

Using condition (2.58) we can formulate the following range theorem.

Theorem 2.5.1. *Given three functions $g_i \in C^{\infty}(\mathbb{R}^2)$, $i = 1, 2, 3$, define $g_{ij} = g_i - g_j$, $i \neq j$. Let $U \subset \mathbb{R}^2$ be an open convex set, and all the foci $x_0^{(i)}$ be outside the closure of U. There exists $f \in C_0^{\infty}(U)$ such that*

$$g_{ij}(x) = \int_{R_i(x)} f dt - \int_{R_j(x)} f dt,\ 1 \leq i, j \leq 3,\ i \neq j, \tag{2.61}$$

if and only if

1. *for all $1 \leq i, j \leq 3$, $i \neq j$, and $x \notin U$ we have:*
    - *(a) $g_{ij}(x) = 0$ if $R_i(x)$ and $R_j(x)$ do not intersect U;*
    - *(b) $\nabla_i g_{ij}(x) = 0$ if $R_i(x)$ intersects U, but $R_j(x)$ does not intersect U;*
    - *(c) $c_{ik}^{\perp}\nabla_j g_{jk}(x) + c_{kj}^{\perp}\nabla_i g_{ik}(x) = 0$, where $k \neq i, j$, if both $R_i(x)$ and $R_j(x)$ intersect U;*
2. *condition (2.58) is satisfied.*

Remark 1. *Note that the theorem does not establish the equalities $g_i(x) = \int_{R_i(x)} f dt$. Instead the range characterization is formulated in terms of the differences g_{ij}.*

Remark 2. *In the theorem we assume that the functions g_i (and the differences g_{ij}) are known for all $x \in \mathbb{R}^2$. If they are known only for $x \in supp\, f$ (i.e. where $\mu_s(x) > 0$, cf. the Introduction), then (2.58) becomes a necessary range condition. This condition is local, so it can be verified for all x where the data are known.*

Proof. Define $f(x)$ using (2.44) and g_{12}, g_{32} (or, using (2.46) and all the g_i). Clearly, $f \in C^\infty$. Conditions 1.a–1.c guarantee that f vanishes outside U. By construction, (2.58) is equivalent to (2.51). Equation (2.51) implies that the function $J_2(x)$ defined by the right-hand side of (2.49) satisfies (2.15), where f is given by (2.44). Pick any x and consider the point $y = x + t\beta_2(x)$. Using conditions 1.a or 1.b, we see that the right-hand side of (2.49) is zero at a point y when $t > 0$ is large enough. Since $f = 0$ outside of U, integrating (2.15) along $R_2(x)$ from $t = \infty$ to $t = 0$ we see that (2.11) holds for all x and $j = 2$, where f is given by (2.44). This implies that equations (2.43) hold for all x. Recall that equations (2.43) can be written in the form

$$\nabla_i \left\{ g_{ij}(x) - \left[\int_{R_i(x)} f dt - \int_{R_j(x)} f dt \right] \right\}, \tag{2.62}$$

where $i = 1, 3$ and $j = 2$. By symmetry, equations (2.62) hold for all $1 \le i, j \le 3$, $i \ne j$. Hence all the differences

$$g_{ij}(x) - \left[\int_{R_i(x)} f dt - \int_{R_j(x)} f dt \right],\ 1 \le i, j \le 3,\ i \ne j, \tag{2.63}$$

are constants. Since U is convex and the foci $x_0^{(j)}$ are outside of U, for each pair i, j we can choose a point x such that both $R_i(x)$ and $R_j(x)$ do not intersect U. From 1.a, $g_{ij} = 0$ for such x. Clearly, $\int_{R_i(x)} f dt = \int_{R_j(x)} f dt = 0$ for such x as well. Hence all the differences in (2.63) are identically zero, and the theorem is proven. $\square$

2.6 Numerical experiments

The main purpose of this section is to provide preliminary numerical testing of the new three-detector inversion formula. Hence we use neither a challenging phantom nor the most realistic simulation parameters. Instead, we simulate a simplified set-up that still resembles the experiment described in section 2.1. Let e_1 and e_2 be the unit vectors along the x_1- and x_2-axes, respectively. We assume that the primary beam is along e_2, and the measurement at each detector is the function

$$g_i(x) = \int_{R_i(x)} f dt + \int_0^\infty f(x - te_2)dt,\ 1 \le i \le 3. \tag{2.64}$$

Clearly, with this choice of g_i we still have $g_{ij} = g_i - g_j$, where g_{ij} satisfy (2.61). In view of the discussion in the Introduction, we assume that the data (2.64) are given only for those x where $f > 0$. The native coordinates in our set-up are u_i, $i = 1, 2, 3$, and x_1. Here u_i is either a linear coordinate along the detector if D_i is flat, or an angular variable – if D_i is curved. The variable x_1 describes the x_1-coordinate of the primary beam. Let $G_i(x_1, u_i)$ denote the data function g_i expressed in terms of the native coordinates. Notice that in (2.46) each g_i is differentiated only along β_i. As is easily seen,

$$\nabla_i g_i(x) = (\beta_i \cdot e_1)\frac{\partial G_i(x_1, u_i)}{\partial x_1}, \tag{2.65}$$

where it is assumed that the coordinates (x_1, u_i) correspond to the point x on the left side of (2.65).

In the experiments presented below we assume that the data are given in native coordinates $G_i(m\Delta x_1, n\Delta u_i)$, $i = 1, 2, 3$. First, the derivatives are computed using (2.65) and finite differences. Then they are interpolated to a required rectangular grid for use in (2.46). The phantom is the superposition of disks of different radii and attenuation f (see Fig. 2.4). The largest disk is of radius 100 and attenuation $f = 1$.The three top disks inside are of radii 20, 16, 10 and attenuation 0.4, -0.2, 0.6, respectively (from left to right). The bottom disk is of radius 30 and attenuation 0.2.

In both experiments $\Delta x_1 = 0.5$.

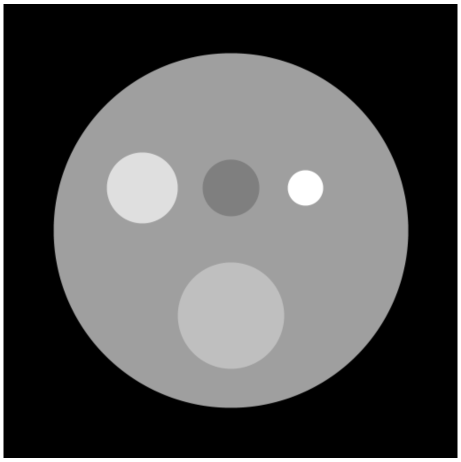

Figure 2.4: Illustration of the phantom used in numerical experiments.

Fig. 2.5 shows the reconstruction results with three flat detectors with $\Delta u_i = 0.5$ for each of them. The corresponding directions are given by $\beta_i = (\cos\theta_i, \sin\theta_i)$, where $\theta_1 = 0°$, $\theta_2 = 45°$, and $\theta_3 = 135°$. The left panel shows the reconstruction from noise-free data, and the right panel shows the reconstruction from noisy data. Noise was simulated as a Gaussian random variable with the standard deviation of 10^{-3} times the maximum value in the sinogram. For improved noise stability, images reconstructed by applying inversion formula (2.46) were smoothed. Cross-sections through the reconstructions are shown in Fig. 2.6. Fig. 2.7 shows the corresponding (noise-free) detector data.

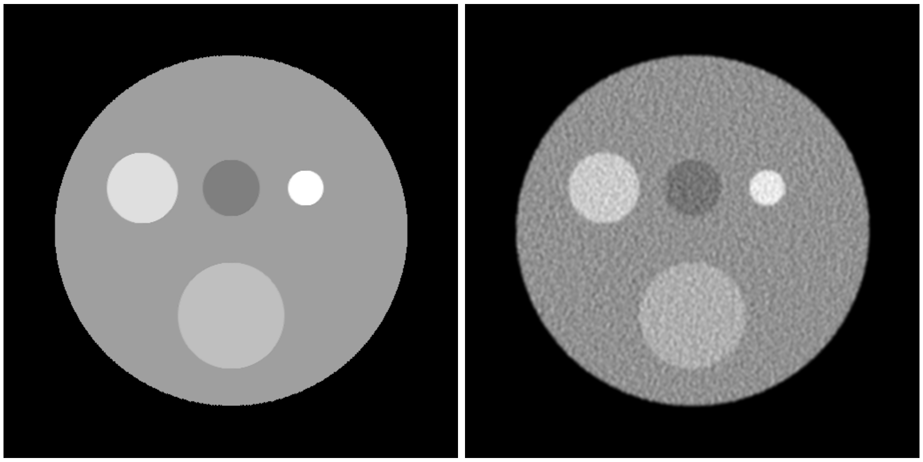

Figure 2.5: Reconstruction results when the detectors are flat. Left panel - reconstruction from noise-free data, right panel - reconstruction from noisy data.

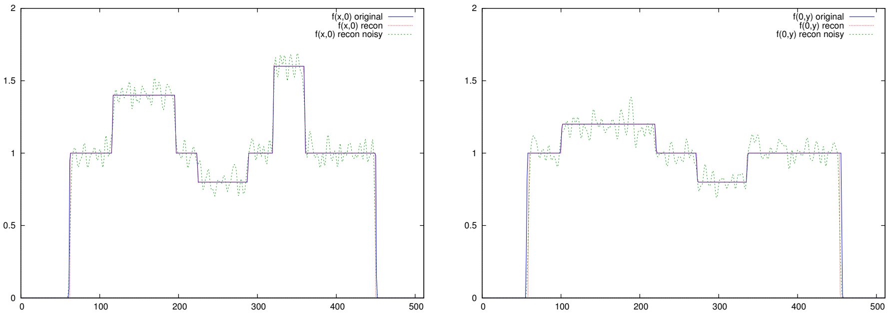

Figure 2.6: Cross-sections through the results shown in Fig 2.5. Left panel - horizontal cross-section through the centers of the three smaller balls, right panel - vertical cross-section through the center. Blue - original profile, red - profile reconstructed from exact data, green - profile reconstructed from noisy data.

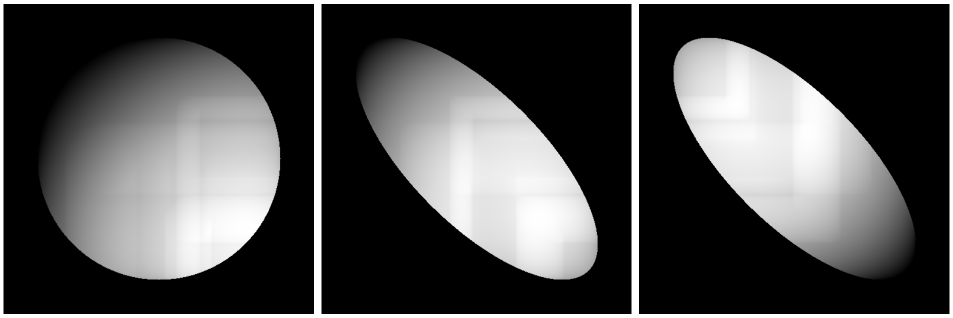

Figure 2.7: Detector data in the case of three flat detectors with directions determined by $\theta_1 = 0°$, $\theta_2 = 45°$, and $\theta_3 = 135°$ (from left to right). The horizontal axis corresponds to the position of the incident beam, and the vertical axis is the variable along the face of detector.

Fig. 2.8 shows the results with three curved detectors. We assumed that the detectors are convex, and their foci are located at the points $r(\cos\theta_i, \sin\theta_i)$, where $r = 256$ and $\theta_1 = 0°$, $\theta_2 = 45°$, and $\theta_3 = 135°$. Clearly, the actual radius of the detector surface is irrelevant. We assumed that the surface of each detector covers an arc of 1 radian, which is symmetric about the line segment connecting the origin and the focus. There were 512 detector elements, so the step-size along the detector angular variable turned out to be $\Delta u_i = 1.953 \cdot 10^{-3}$rad for all i. The left panel of Fig. 2.8 shows the reconstruction from noise-free data, and the right panel shows the reconstruction from noisy data. Noise was simulated as a Gaussian random variable with the standard deviation of 10^{-3} times the maximum value in the sinogram. For improved noise stability, images reconstructed by applying inversion formula (2.46) were smoothed. Cross-sections through the reconstructions are shown in Fig. 2.9. Fig. 2.10 shows the corresponding (noise-free) detector data.

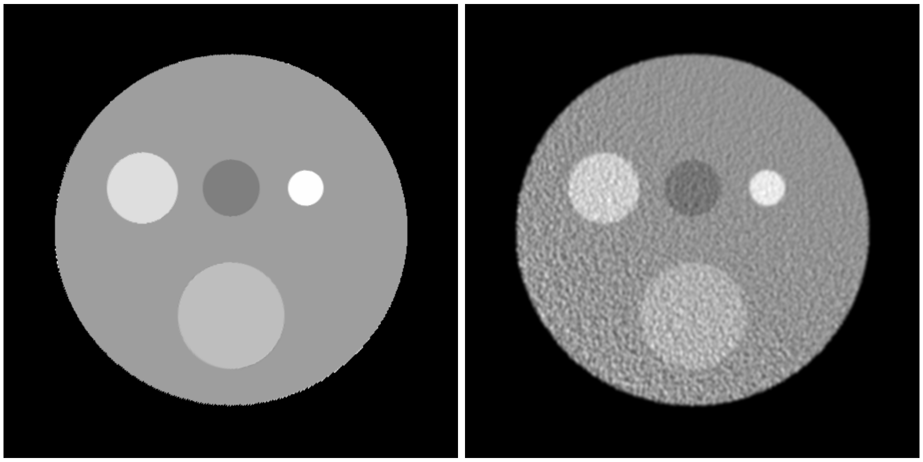

Figure 2.8: Reconstruction results when the detectors are convex. Left panel - reconstruction from noise-free data, right panel - reconstruction from noisy data.

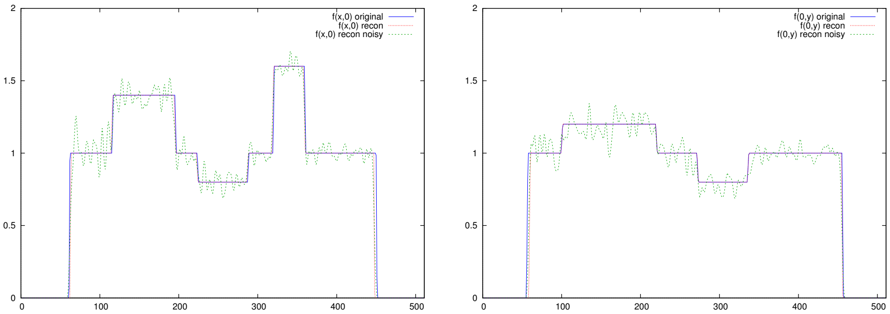

Figure 2.9: Cross-sections through the results shown in Fig 2.8. Left panel - horizontal cross-section through the centers of the three smaller balls, right panel - vertical cross-section through the center. Blue - original profile, red - profile reconstructed from exact data, green - profile reconstructed from noisy data.

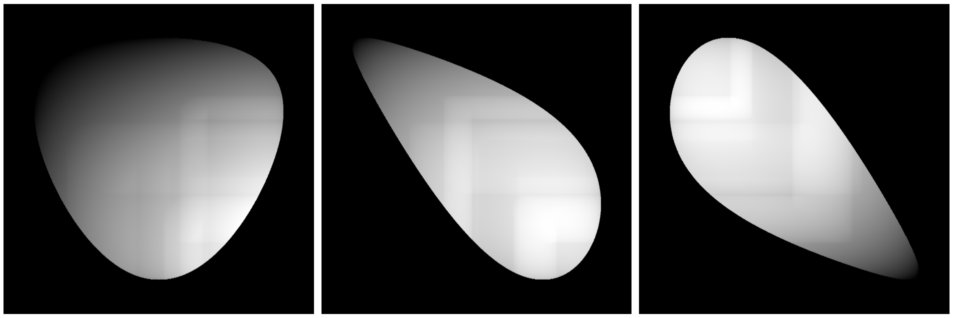

Figure 2.10: Detector data in the case of three curved detectors located at $\theta_1 = 0°$, $\theta_2 = 45°$, and $\theta_3 = 135°$ (from left to right). The horizontal axis corresponds to the position of the incident beam, and the vertical axis is the angular variable along the face of the detector.

CHAPTER 3: TWO GENERALIZATIONS: ENERGY-DEPENDENT ATTENUATION AND MORE THAN THREE DETECTORS.

3.1 Introduction.

In this chapter we continue to study various approaches to inverting the BRT. In addition to the single scattering approximation, another key assumption on which the BRT is based is that the attenuation coefficient of the medium before and after scattering remains the same (see [KK13, ZSM14]). As is well known, x-rays loose their energy after Compton scattering. Note that Compton scattering is the most prevalent type of scattering for a range of energies common in medical imaging [Pod10]. Moreover, the energy loss depends on the scattering angle [Pod10]. Since the attenuation coefficient μ depends on the energy of x-rays, the values of μ before and after scattering are different. In [KK13, ZSM14] the benefits of having more than two detectors are discussed. It is easy to see that when there are three or more detectors one should distinguish not only between μ's that are "seen" by x-rays before and after scattering, but also between μ's that are "seen" by x-rays traveling towards different detectors.

The main thrust of this work is inversion of the BRT with $N \geq 3$ detectors under the assumption that the attenuation coefficient is a linear function of energy in the range of relevant energies. When the number of detectors is greater than four, we derive a family of inversion formulas. We also find the optimal formula, which provides the best stability with respect to noise in the data. If $N = 4$, the family collapses into a single formula and no optimization is possible. If the dependence of μ on energy is neglected, our family is analogous to the one obtained in [ZSM14]. In this case the minimum number of detectors sufficient for inversion is three. When μ is independent of energy and $N = 3$, we recover the formula that was first found in [KK13]. Besides inversion formulas, we develop iterative reconstruction algorithms that are based on minimizing a functional which consists of a data fidelity term and a regularizer. Our motivation is that the presence of a regularizer will improve further the noise stability of BRT inversion.

The work is organized as follows. In Section 3.2 we introduce the BRT with energy-dependent attenuation and derive a family of inversion formulas. In Section 3.2.2 we discuss how to find the formula, which is the most stable with respect to noise in the data. In Section 3.2.3 we consider a particular case when μ does not depend on energy. Even though in this case the resulting inversion formulas are similar to those obtained in [ZSM14], optimization with respect to noise is new. Iterative reconstruction algorithms are described in Section 3.3. We start with reconstruction from a complete data set and consider energy independent and energy dependent μ's in Section 3.3.1. In Section 3.3.2 we consider reconstruction of the region of interest (ROI) from local data when μ is energy independent. Results of testing of the inversion formulas and iterative algorithms are reported in Section 2.6. Note that the numerical experiments presented in this work are by no means exhaustive, and are designed only as a proof-of-principle study. More detailed experiments should be performed in the future. Finally, some generalizations and directions for future research are discussed in Section 4.

3.2 Energy-dependent reconstruction of BRT

3.2.1 Inversion Formula

Consider an x-ray source moving along the positive direction of the x-axis. The position of the source is denoted by A. We assume that the source emits an infinitely thin x-ray beam in the positive direction of the y-axis. At every point of its path inside the object the beam is scattered in all directions. Suppose that there are N detectors $\mathcal{D}_j$, $j = 1, \dots, N$, which are flat and collimated.

This means that each $\mathcal{D}_j$ detects radiation propagating along a fixed direction β_j. Pick any source position A and any point $D_j \in \mathcal{D}_j$. By construction, the pair (A, D_j) determines a unique scattering point B such that the radiation propagating along the broken ray ABD_j is detected at the location D_j (see Figure 3.1).

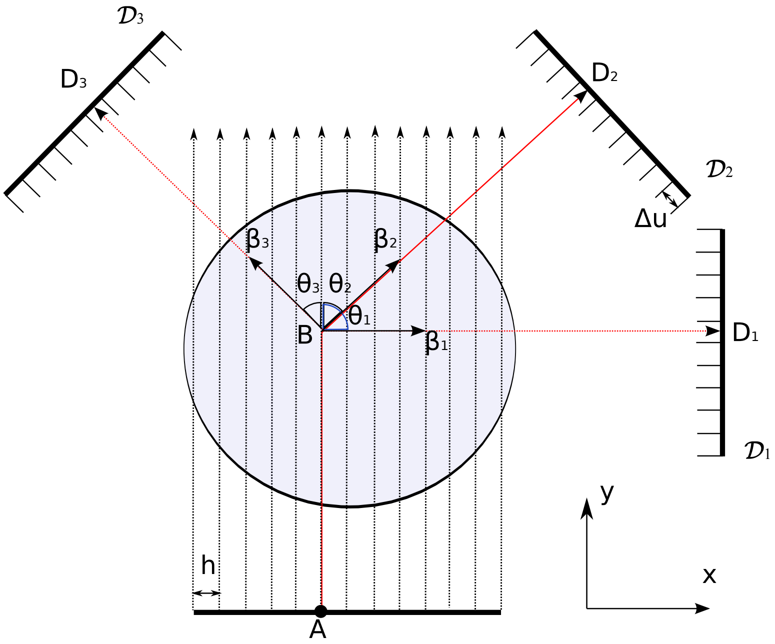

Figure 3.1: Illustration of parallel beam geometry.

The energy of the scattered photons depends on the scattering angle θ and the energy E_{src} of the incident x-ray beam according to the Compton formula (formula [3-3] in [Bus02])

$$E(\theta) = \frac{E_{\text{src}}}{1 + \dfrac{E_{\text{src}}}{m_e c^2}(1 - \cos(\theta))}, \tag{3.1}$$

where m_e is the electron rest mass and c is the speed of light. Let θ_j denote the angle between the positive direction of the y-axis and $\vec{\beta}_j$ (see Figure 3.1). Let the minimal and maximal energy of scattered photons observed by the detectors be $E_{\min}$ and $E_{\max}$, respectively:

$$E_{\min} = \min_{j=1,\dots,N} E(\theta_j), \quad E_{\max} = \max_{j=1,\dots,N} E(\theta_j). \tag{3.2}$$

To take Compton energy shifts into account in the reconstruction algorithm we assume that the dependence of the attenuation coefficient $\mu(B, E)$ on energy E is linear at every point B inside the object (or, inside the region of interest (ROI)) for all $E \in [E_{\min}, E_{\max}]$. Choose some $E_0 \in (E_{\min}, E_{\max})$ and consider the linear approximation:

$$\mu(B, E) \approx \mu(B) + (E - E_0) \cdot \nu(B), \quad E \in (E_{\min}, E_{\max}), \tag{3.3}$$

where $\mu(B)$ is the attenuation coefficient at the energy E_0.

Let $J_{\text{in}}(A)$ be the intensity of the incoming beam and $\Delta E_j := E(\theta_j) - E_0$. The intensity of radiation measured at a point $D \in \mathcal{D}_j$ equals

$$\begin{aligned} J_{\text{out}}(D) =& J_{\text{in}}(A) \cdot K(\theta_j) \cdot \mu_s(B, E_{\text{src}}) \\ & \times \exp\left(-\int_{AB} \mu(x, E_{\text{src}}) dx - \int_{BD} [\mu(x) + \Delta E_j \nu(x)] dx \right), \end{aligned} \tag{3.4}$$

where $\mu_s(B, E_{\text{src}})$ is the scattering coefficient at the point B for the energy E_{src}, and $K(\theta)$ is the normalized Klein-Nishina function (see e.g. (7.95) in [Pod10] or [FSM09, FMS11, KK13]). We assume that $\mu_s(B, E_{\text{src}})$ is positive at every point inside the object (or, inside the ROI). Denoting

$$I_0 = \int_{AB} \mu(x, E_{\text{src}}) dx, \quad G_j(B) = -\ln(J_{\text{out}}(D_j)/[J_{\text{in}}(A) K(\theta_j)]), \tag{3.5}$$

we get from (3.4)

$$G_j(B) = \int_{BD_j} \mu(x)dx + \Delta E_j \int_{BD_j} \nu(x)dx + I_0(B) - \ln \mu_s(B). \tag{3.6}$$

Since $J_{\text{out}}(D_j)$ is measured, $J_{\text{in}}(A)$, $K(\theta_j)$ are known, and B is uniquely determined from A and D_j, we can view the function $G_j(B)$ as our data.

Let ∇_j denote the derivative in the direction $\vec{\beta}_j$. Applying ∇_j to (3.6) and using that θ_j does not change along the direction β_j, we get

$$\nabla_j G_j = -\mu(B) - \Delta E_j \nu(B) + \nabla_j (I_0(z) - \ln \mu_s(z))\big|_{z=B} . \tag{3.7}$$

Take a linear combination of (3.7) for all $j = 1, \ldots, N$

$$\sum \xi_j \nabla_j G_j = -\mu(B) \sum \xi_j - \nu(B) \sum \xi_j \Delta E_j + \sum \xi_j \; \nabla_j (I_0(z) - \ln \mu_s(z))\big|_{z=B} , \tag{3.8}$$

where ξ_j are some coefficients. The last term on the right in (3.8) is unknown. To get rid of it we can find ξ_j such that $\sum \xi_j \nabla_j = 0$. Let β_{j1} and β_{j2} be the projections of β_j onto the x- and y-axes, respectively. Clearly, $\nabla_j = \beta_{j1}\partial_x + \beta_{j2}\partial_y$, so the constraints on $\{\xi_j\}$ become:

$$\sum \xi_j \beta_{j1} = 0, \quad \sum \xi_j \beta_{j2} = 0. \tag{3.9}$$

Next we can solve (3.8) for μ and ν. Set

$$\sum \xi_j \Delta E_j = 0, \quad \sum \xi_j = 1, \tag{3.10}$$

and let the solution of (3.9) and (3.10) be denoted $\xi_1 = C_1, \ldots, \xi_N = C_N$. The inversion formula for μ is

$$\mu(B) = -\sum C_j \nabla_j G_j. \tag{3.11}$$

Alternatively, we set

$$\sum \xi_j \Delta E_j = 1, \quad \sum \xi_j = 0. \tag{3.12}$$

Let the solution of (3.9) and (3.12) be denoted $\xi_1 = B_1, \ldots, \xi_N = B_N$. The inversion formula for ν is given by

$$\nu(B) = -\sum B_j \nabla_j G_j. \tag{3.13}$$

In principle, the system of equations (3.9) together with either (3.10) or (3.12) may have no solution in certain cases. In our experience, this never happened for reasonable detector positions and typical energies in the 50 KeV–1.5 MeV range.

3.2.2 Noise Minimization

When there are more than four detectors, the systems that determine C_j and B_j are underdetermined. In this case we can use the available degrees of freedom to optimize with respect to noise stability. Consider reconstructing the attenuation function at an energy $E = E_0 + \Delta E$ at some point B inside the object. In all formulas in this section we assume that the point B is fixed, so it is omitted from notation. Using (3.3) and equations (3.11), (3.13) we have

$$\begin{aligned}\mu(E) = \mu(E_0) + \nu \Delta E &= -\sum C_j \nabla_j G_j - \Delta E \sum B_j \nabla_j G_j \\ &= -\sum (C_j + \Delta E B_j) \nabla_j G_j.\end{aligned} \tag{3.14}$$

Let the k-th source position be $A_k = A_0 + kh$, where h is the source step size (see Figure 3.1).

Let the l-th detection point on $\mathcal{D}_j$ be $D_{jl} = D_{j0} + l\Delta u$, where Δu is the size of the detector pixel. For simplicity we assume that all detectors have the same resolution Δu. Let $G_j(k,l)$ be the measurement of G_j at the l-th detector pixel for the k-th source position. Consider a two-point finite difference approximation of the directional derivative ∇_j:

$$\nabla_j G_j(k+\frac{1}{2},l) \approx \frac{G_j(k+1,l)-G_j(k,l)}{h}\sin(\theta_j). \tag{3.15}$$

The actual data $G_j(k,l)$ can be written in the form:

$$G_j(k,l) = G_j^{(0)}(k,l) + \epsilon_{jkl}, \tag{3.16}$$

where $G_j^{(0)}(k,l)$ is the exact value of the BRT, and ϵ_{jkl} represents noise. We assume that ϵ_{jkl} are independent, normally distributed, with zero mean and standard deviation $\hat{\sigma}_{jkl}$. The random variable defined by the right-hand side of (3.15) has variance

$$\sigma_{jkl}^2 = \frac{\hat{\sigma}_{j,k+1,l}^2 + \hat{\sigma}_{j,k,l}^2}{h^2}\sin^2(\theta_j) \tag{3.17}$$

Since the reconstruction point B is fixed, the values of k and l in (3.17) are fixed as well. Note also that the values of k and l in (3.17) do not depend on the value of j. Hence, for simplicity, in this section we drop the subscripts k and l from notation. Assuming that the standard deviation σ_j of noise in $\nabla_j G_j$ is known and using the linearity of (3.14), the variance of the error in the reconstruction of $\mu(E)$ is given by

$$\sigma^2(E) = \overline{(\mu_{\text{rec}}(E) - \mu_{\text{exact}}(E))^2} = \sum (C_j + \Delta E B_j)^2 \sigma_j^2. \tag{3.18}$$

Here $\mu_{\text{rec}}(E)$ and $\mu_{\text{exact}}(E)$ are the reconstructed and exact values of the attenuation coefficient at the energy E, respectively, and the overbar denotes taking expectation.

In order to minimize the error in the reconstruction of μ over the entire range $[E_{\min}, E_{\max}]$ and using the linearity of expectation, we minimize the functional

$$\begin{aligned}\sigma^2 &= \sigma^2(E_{\max}) + \sigma^2(E_{\min})\\ &= \sum \left\{(C_j + \Delta E_1 B_j)^2 + (C_j + \Delta E_2 B_j)^2\right\} \sigma_j^2\\ &= \sum \left\{2C_j^2 + 2C_j B_j(\Delta E_1 + \Delta E_2) + B_j^2(\Delta E_1^2 + \Delta E_2^2)\right\} \sigma_j^2, \end{aligned} \tag{3.19}$$

where $\Delta E_1 = E_{\max} - E_0$ and $\Delta E_2 = E_{\min} - E_0$.

The systems (3.9), (3.10) and (3.9), (3.12) can be written in vector form as

$$\vec{C} \cdot \vec{b}_1 = 0 \qquad \vec{B} \cdot \vec{b}_1 = 0 \tag{3.20}$$

$$\vec{C} \cdot \vec{b}_2 = 0 \qquad \vec{B} \cdot \vec{b}_2 = 0 \tag{3.21}$$

$$\vec{C} \cdot \vec{1} = 1 \qquad \vec{B} \cdot \vec{1} = 0 \tag{3.22}$$

$$\vec{C} \cdot \vec{E} = E_0 \qquad \vec{B} \cdot \vec{E} = 1, \tag{3.23}$$

where $(\vec{b}_1)_j = \beta_{j1}$, $(\vec{b}_2)_j = \beta_{j2}$, $\vec{1} = (1, \ldots, 1)^T$ and $\vec{E} = (E(\theta_1), \ldots, E(\theta_N))$. The two systems (3.20)–(3.23) can be written jointly as a single vector equation

$$Q\vec{p} = \vec{r}, \tag{3.24}$$

where

$$Q = \begin{bmatrix} b_{1,1} & \dots & b_{1,N} & 0 & \dots & 0 \\ b_{2,1} & \dots & b_{2,N} & 0 & \dots & 0 \\ 1 & \dots & 1 & 0 & \dots & 0 \\ E_1 & \dots & E_N & 0 & \dots & 0 \\ 0 & \dots & 0 & b_{11} & \dots & b_{1,N} \\ 0 & \dots & 0 & b_{21} & \dots & b_{2,N} \\ 0 & \dots & 0 & 1 & \dots & 1 \\ 0 & \dots & 0 & E_1 & \dots & E_N \end{bmatrix}, \qquad \vec{p} = \begin{bmatrix} C_1 \\ \vdots \\ C_N \\ B_1 \\ \vdots \\ B_N \end{bmatrix}, \qquad \vec{r} = \begin{bmatrix} 0 \\ 0 \\ 1 \\ E_0 \\ 0 \\ 0 \\ 0 \\ 1 \end{bmatrix}. \tag{3.25}$$

In terms of this notation (3.19) becomes

$$\sigma^2 = \langle A\vec{p}, \vec{p} \rangle \to \min. \tag{3.26}$$

Here A is a symmetric matrix given by

$$A = \begin{bmatrix} A_1 & A_2 \\ A_2 & A_3 \end{bmatrix}, \tag{3.27}$$

where $A_1 = \operatorname{diag}(2\sigma_j^2)$, $A_2 = \operatorname{diag}([\Delta E_1 + \Delta E_2]\sigma_j^2)$, $A_3 = \operatorname{diag}([\Delta E_1^2 + \Delta E_2^2]\sigma_j^2)$ for $j = 1, \dots, N$.

Let R by any square matrix such that $A = R^T R$. Since $\Delta E_1 \neq \Delta E_2$ and all $\sigma_j > 0$, (3.19) immediately implies that A is non-singular. Thus R is non-singular as well. Denoting $\vec{t} := R\vec{p}$, we rewrite (3.26) and (3.24) as follows:

$$\sigma^2 = \|\vec{t}\|^2 \to \min, \quad (QR^{-1})\vec{t} = \vec{r}. \tag{3.28}$$

The solution to (3.28) is given by the pseudoinverse

$$\vec{t}_{\mathrm{opt}} = \tilde{Q}^T(\tilde{Q}\tilde{Q}^T)^{-1}\vec{r}, \quad \tilde{Q} := QR^{-1}. \tag{3.29}$$

Simplifying we find after elementary transformations:

$$\vec{p}_{\mathrm{opt}} = R^{-1}\vec{t}_{\mathrm{opt}} = Q^{+}\vec{r}, \tag{3.30}$$

where we denoted $Q^{+} = A^{-1}Q^T(QA^{-1}Q^T)^{-1}$. Also, we obtain

$$\sigma^2_{\mathrm{opt}} = \langle A\vec{p}_{\mathrm{opt}}, \vec{p}_{\mathrm{opt}}\rangle = \left\langle AQ^{+}\vec{r},\ Q^{+}\vec{r}\right\rangle = \left\langle (QA^{-1}Q^T)^{-1}\vec{r},\ \vec{r}\right\rangle. \tag{3.31}$$

3.2.3 The case of energy-independent attenuation

If the detectors are placed in such a way that all the scattering angles θ_j are small or if the attenuation growth rate ν is negligibly small in the range $[E_{\min}, E_{\max}]$, then we can neglect the energy shift ΔE in (3.4) and the following formulas. In this case the reconstruction formula (3.11) remains the same. The only difference is that we do not need to use the first equation in (3.10). This reduces the number of conditions on C_j by one, and the minimum number of detectors that allows exact reconstruction is three. The resulting family of inversion formulas is equivalent to the one in [ZSM14].

When there are more than three detectors, we can use the technique from Section 3.2.2 to minimize noise in the reconstruction. Note that this time we do not have the first equation in (3.23). The system to determine the coefficients C_j becomes

$$Q_1\vec{C} = \vec{r}_1, \quad Q_1 := \begin{bmatrix} b_{1,1} & \dots & b_{1,N} \\ b_{2,1} & \dots & b_{2,N} \\ 1 & \dots & 1 \end{bmatrix}, \ \vec{r}_1 = \begin{bmatrix} 0 \\ 0 \\ 1 \end{bmatrix}. \tag{3.32}$$

Again, making the assumption that noise in the data is independent and normally-distributed, the variance of noise in the reconstructed $\mu(B)$ is given by

$$\sigma^2 = \sum C_j^2 \sigma_j^2 = \|\Sigma C\|_2^2, \tag{3.33}$$

where $\Sigma = \mathrm{diag}(\sigma_j)$. Denoting $\vec{t} = \Sigma^{1/2}\vec{C}$ and arguing similarly to (3.28)–(3.31) we obtain that the vector $\vec{C}$ that minimizes (3.33) and satisfies (3.32) is given by:

$$\vec{C}_{\text{opt}} = \Sigma^{-2} Q_1^T (Q_1 \Sigma^{-2} Q_1^T)^{-1} \vec{r}_1. \tag{3.34}$$

We note that in the case of only three detectors the formula above reduces to

$$\vec{C}_{\text{opt}} = {Q_1}^{-1} \vec{r}_1. \tag{3.35}$$

This is a unique solution, and no optimization is possible. The corresponding inversion formula is equivalent to the one in [KK13].

3.3 Iterative Reconstruction

It turns out that the sensitivity of the exact method (3.11) to noise in the data is still high even when the optimal constants C_j are used. To reduce the noise sensitivity we develop an iterative reconstruction algorithm based on functional minimization. We choose this approach because of its ability to include a regularization functional.

3.3.1 Global Reconstruction

In this section we assume that the global data are known, i.e. any broken ray with the scattering point B inside the object is measured. Consider first the case of energy-independent attenuation.

Using that the values $K(\theta_j)$ are known in (3.6) and setting $\nu \equiv 0$ in (3.6), we obtain from (3.5) and (3.6) that our data are

$$\tilde{G}_j(A, D_j) = \left(\int_{AB} + \int_{BD_j} \right) \mu(x) dx - \ln \mu_s(B). \tag{3.36}$$

As opposed to the previous section, now the data are parametrized by "native coordinates" (A, D_j), and not by interior points B. Note also another difference between the approaches in this and the preceding sections. In the preceding section by choosing the coefficients ξ_j appropriately, we eliminated the need to compute $\ln \mu_s(B)$. In this section we need to recover both $\mu(B)$ and $\ln \mu_s(B)$ for all B inside the object.

Our method is based on minimizing the functional

$$F(u, v) = \frac{1}{2} \left\| P^{(1)}u + P^{(2)}v - b \right\|_2^2 + \lambda_u R(u) + \lambda_v R(v). \tag{3.37}$$

Here $u = (u_1, \ldots, u_N)^T$ and $v = (v_1, \ldots, v_N)^T$ are the vectors that represent the values of $\mu(B)$ and $\ln \mu_s(B)$, respectively, on a regular grid covering the object, N is the total number of grid nodes, $P^{(1)}, P^{(2)}$ are projection matrices, b represents the data, R is a regularization functional, and $\lambda_u, \lambda_v > 0$ are some constants.

In the experiments we assume that the attenuation coefficient $\mu(B)$ and the scattering coefficient $\mu_s(B)$ both equal zero when B is outside the object. Clearly, if A and D_j are such that $\mu_s(B) = 0$ for the corresponding vertex B, equation (3.36) does not apply. Fortunately, these "unacceptable" broken rays can be detected, because in their case the original data in (3.4) equals zero. Thus, at the very beginning of the algorithm we detect all broken rays whose vertex B is outside the object and exclude the corresponding components of the vectors u and v from the optimization problem. In other words, we first find the support of the object and then discard the grid nodes located outside the object. In what follows, N denotes the number of remaining nodes.

For a pair of indices m, n, $P^{(1)}_{mn}$ is the weight with which the image element u_n contributes to the projection data along the m-th broken ray. $P^{(1)}_{mn}$ is computed using bilinear interpolation and integrating along the section of the m-th broken ray that is affected by the corresponding image element. Similarly, $P^{(2)}_{mn}$ is the weight with which the image element v_n contributes to the projection data along the m-th broken ray. $P^{(2)}_{mn}$ equals (-1) times the value of the n-th bilinear interpolating function (i.e., the function which is centered at the n-th grid node) computed at the vertex B of the m-th broken ray. To summarize, given two row-vectors $P^{(1)}_m$ and $P^{(2)}_m$, the value $\left\langle P^{(1)}_m, u \right\rangle + \left\langle P^{(2)}_m, v \right\rangle$ is the result of forward projecting the pair (u, v) along the m-th broken ray. The vector b contains the data, and $\left\| P^{(1)}\tilde{u} + P^{(2)}\tilde{v} - b \right\|_2$ is a measure of how well the simulated data corresponding to an intermediate image $(\tilde{u}, \tilde{v})$ approximates b.

For computations we use a regularizer based on total variation. To compute $R(u)$, we regard u as a two-dimensional array $U_{i,j}$ and use a conventional formula for discrete total variation in two dimensions (see e.g. [Get12]):

$$R(u) = \sum_{i,j} \big\{ (U_{i+1,j} - U_{i,j})^2 + (U_{i,j} - U_{i-1,j})^2 + (U_{i,j+1} - U_{i,j})^2 + (U_{i,j} - U_{i,j-1})^2 + \varepsilon \big\}^{1/2}, \tag{3.38}$$

where the summation is over all interior nodes of the grid. Here ε is a small positive number, which ensures the differentiability of $R(u)$. The computation of $R(v)$ is done in an analogous manner.

To minimize the functional in (3.37) numerically (note that $F(u, v)$ is convex) we use the method of gradient descent with exact line search. Inversion formula (3.11) and the discussion in Section 3.2.3 show that $\mu(B)$ can be uniquely reconstructed from the data. Once $\mu(B)$ is known, $\ln \mu_s(B)$ can be found as well by substituting $\mu(B)$ into (3.36). Hence the data $\tilde{G}_j(A, D_j)$ are sufficient for the recovery of both $\mu(B)$ and $\ln \mu_s(B)$, and by minimizing the functional in (3.37) we can find reasonable approximations to those functions.

In the case of energy-dependent attenuation, a similar iterative algorithm can be derived. To reduce the number of unknowns we assume that the linear dependence of attenuation on energy holds over the entire interval $[E_{\min}, E_{\text{src}}]$ and substitute $E_0 = E_{\text{src}}$ in (3.3). Using (3.6) we may assume that our data are

$$\tilde{G}_j(A, D_j) = \left(\int_{AB} + \int_{BD_j} \right) \mu(x)dx + (E_j - E_{\text{src}}) \int_{BD_j} \nu(x)dx - \ln \mu_s(B). \tag{3.39}$$

The analogue of (3.37) becomes

$$F(u, v, w) = \frac{1}{2} \left\| P^{(1)}u + P^{(2)}v + P^{(3)}w - b \right\|_2^2 + \lambda_u R(u) + \lambda_v R(v) + \lambda_w R(w). \tag{3.40}$$

Here u, v, $P^{(1)}$, $P^{(2)}$ are the same as in (3.37), the vector w represents the values of $\nu(B)$ on the grid, and the projection matrix $P^{(3)}$ discretizes the second integral in (3.39).

Since the typical values of ν are several orders of magnitude smaller than the typical values for μ, straightforward discretization of the integral $\int_{BD_j} \nu(x)dx$ leads to a very slow convergence of the gradient descent method. To accelerate convergence, the components of the vector w are taken to be the values of $\kappa\nu$ for some constant κ. This constant is chosen so that the vectors v and w are approximately of the same magnitude. Of course, the elements of the matrix $P^{(3)}$ are adjusted accordingly.

3.3.2 Interior Reconstruction

Let U be an open convex set inside the object, we call U the region of interest (ROI). Sometimes one is interested in reconstructing $\mu(B)$ only inside the ROI from local data. The latter is defined as a collection of integrals (3.4) along the broken rays with the vertex inside the ROI. In this section we construct an iterative algorithm for computing $\mu(B)$, $B \in U$. We will consider only the case of energy-independent attenuation.

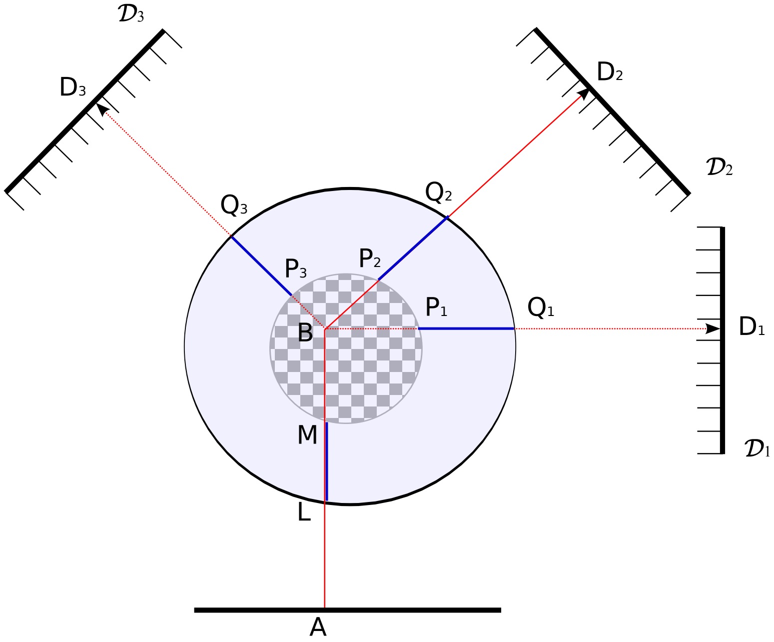

Figure 3.2: Illustration of geometry of local iterative reconstruction.

Consider Figure 3.2, where the ROI is shown as a small disc with checkerboard pattern. Pick any broken ray ABD_j, $D_j \in \mathcal{D}_j$, with the vertex B inside U. We introduce the following notations: L and M are the points where the incoming x-ray beam AB enters the object and the ROI, respectively; P_j and Q_j are the points where the scattered beam BD_j exits the ROI and the object, respectively. Clearly, given A and D_j, the points L, M, P_j, Q_j are determined uniquely.

Rewrite (3.36) in the form

$$\tilde{G}_j(A, D_j) = \int_{LM} \mu(x)dx + \left(\int_{MB} + \int_{BP_j}\right) \mu(x)dx + \int_{P_jQ_j} \mu(x)dx - \ln \mu_s(B). \qquad (3.41)$$

In addition to the unknowns $\mu(B)$ and $\ln \mu_s(B)$, $B \in U$, that we had to find in the global case, we have to determine the unknowns $\psi_{\text{in}}(A) := \int_{LM} \mu(x)dx$ and $\psi_{\text{out}}(D_j) := \int_{P_jQ_j} \mu(x)dx$. As is seen from Figure 3.2, ψ_{in} depends only on the position of the source A, and ψ_{out} depends only on the detection point D_j. The corresponding functional is completely analogous to the one in (3.37). We just add two projection matrices corresponding to ψ_{in} and ψ_{out} and two TV-based regularization terms. Since ψ_{in} and ψ_{out} depend on a single variable (A or D_j), these regularization terms use one-dimensional TV. Likewise, the corresponding projection matrices are computed using linear (rather than bi-linear) interpolation.

Note that the inversion formula (3.11) is local, i.e. one can recover $\mu(B)$ uniquely from the local data. The remaining unknowns: $\ln \mu_s(B)$, ψ_{in}, and ψ_{out} can no longer be recovered, so our iterative algorithm guarantees accurate values only for μ, but not for the other quantities.

To speed up the convergence, we reconstruct $\kappa_{\text{in}}(A)\psi_{\text{in}}(A)$ and $\kappa_{\text{out}}(D_j)\psi_{\text{out}}(D_j)$ instead of $\psi_{\text{in}}(A)$ and $\psi_{\text{out}}(D_j)$. Here $\kappa_{\text{in}}(A)$ and $\kappa_{\text{out}}(D_j)$ are some pre-selected functions that equalize the magnitudes of the unknowns. We tried several candidates: identical 1, the reciprocal of the length of the segments LM and P_jQ_j, respectively, etc. Experimentally, in the case of a disk-shaped ROI, the fastest convergence was observed when the weights were around $1/5$th of the radius of the ROI.

3.4 Numerical experiments

In this section all linear sizes are given in arbitrary (but fixed) units. For the numerical experiments we use a 4-in-1 disc phantom similar to the one in [KK13], see Figure 3.3. The phantom is a superposition of a bigger background disk and four smaller disks of various sizes. For the bigger disk the radius equals $R = 100$, $\mu = 1.0$ and $\nu = 6.8 \cdot 10^{-6}$. The radii of the three smaller disks on top are 20, 16 and 10 (left-to-right), and their values of μ are 1.4, 0.8, and 1.6 respectively. For the lower disk $R = 30$ and $\mu = 1.2$. The value of ν for the four smaller disks is 10^{-6}. In those cases when the attenuation coefficient depends on energy, we assume that this dependence is linear and the values of μ given here are at the energy of the incident beam E_{src}=1.25MeV.

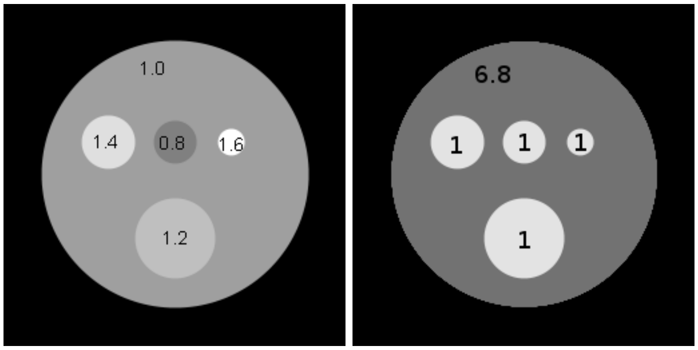

Figure 3.3: 4-in-1 disk phantom. Left panel – distribution of μ at E_{src}, right panel – distribution of ν. The values of ν are multiplied by 10^6 for convenience.

Since the scattering coefficient is not important for reconstruction of the attenuation coefficient as long as it is positive, its value is taken to be equal to 1. In the cases of energy-independent and energy-dependent attenuation, the data are simulated using (3.36) and (3.39), respectively. The simulated detectors are all of length 256 with 256 detector elements each. The source path range is also of length 256, and the source step size equals 1. Thus, $\Delta u = h = 1$ (see Figure 3.1). In some experiments we use four detectors, and in others – five. When there are four detectors, they are located at -90, -45, 45 and 135 degrees. When there are five detectors, they are located at -135, -90, -45, 45 and 135 degrees. These are the values of $\theta_1, \ldots, \theta_N$, cf. Figure 3.1. Using (3.1) we find that in both cases the range of energies of scattered photons registered by the detectors is $[E_{\min}, E_{\max}]$, where $E_{\min} \approx 242\text{KeV}$ and $E_{\max} \approx 729\text{KeV}$.

In the experiments with noisy data we simulate noise as an additive, independent, normally distributed random variable $\mathcal{N}(0, \hat{\sigma}_j)$ with standard deviation $\hat{\sigma}_j = c \cdot F_j$. Here F_j is the maximum value of the noiseless measurements on the jth detector:

$$F_j = \max_{k,l} \tilde{G}_j(k, l), \tag{3.42}$$

where k and l are the indices describing the source and detector element positions, respectively (see the paragraph following (3.14)), and c is a constant that controls the strength of noise. If, for example, $c = 0.001$, we say that the data are contaminated by 0.1% noise.

The reconstructions are done on a 256x256 grid with step-size 1 along each axis.

3.4.1 Noise minimization when attenuation is energy-independent.

To test the noise minimization technique derived in Section 3.2.3 we make a reconstruction of the 4-in-1 disc phantom in the case of four detectors. The data are contaminated by the 0.1% noise.

We choose the coefficient C_4 as a free parameter and make a series of reconstructions for different values of C_4 in a small range around its optimal value. Note that in the case of four detectors, once one of the coefficients C_j is fixed, the other three are determined uniquely. For each value of C_4 we make a series of reconstructions for $M = 20$ different data sets. Each of the M data sets is contaminated by a different randomly generated noise sample $\{\epsilon_{jkl}\}$. See Figure 3.4, where one of the M reconstructions for a few values of C_4 are shown.

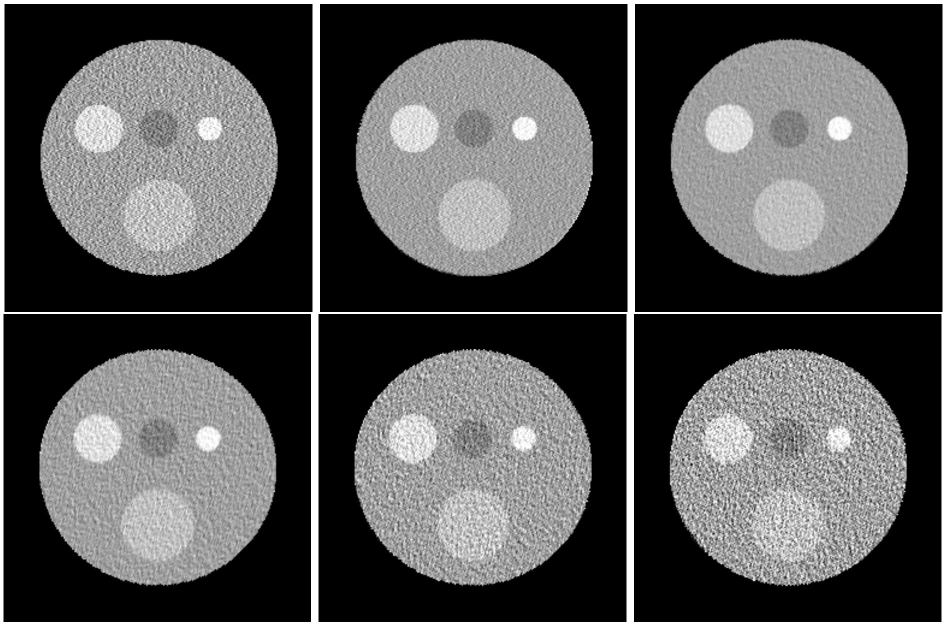

Figure 3.4: Reconstructions from noisy data for different values of the coefficient C_4 in the case of four detectors and energy-independent attenuation. From left to right and from top to bottom: C_4=0, 0.2, 0.4, 0.6, 0.8, 1.0.

To estimate the standard deviation of noise in the reconstructed image we use the following procedure. Let R be the radius of the background disk in the phantom. For all nodes B_{ij} of the reconstruction grid that are located inside the disk with radius $R_0 = 0.8 \cdot R$, we compute sample standard deviation

$$\sigma(B_{ij}) = \left(\frac{1}{M-1} \sum_{m=1}^{M} (\mu_m(B_{ij}) - \bar{\mu}(B_{ij}))^2 \right)^{1/2}, \tag{3.43}$$

where $\mu_m(B_{ij})$ is the reconstructed attenuation for the m-sample at the point B_{ij}, and

$$\bar{\mu}(B_{ij}) = \frac{1}{M} \sum_{m=1}^{M} \mu_m(B_{ij}). \tag{3.44}$$

Then the observed standard deviation of noise in the reconstructed image $\bar{\sigma}$ is taken to be the average of the estimates (3.43).

We also compute theoretically predicted standard deviation σ using the formula (3.33). Note that (3.33) applies for a given grid node B_{ij} only if B_{ij} coincides with the vertex of the broken ray determined by a source position $A_{k+1/2}$ and detection point $D_l \in \mathcal{D}_j$ (cf. (3.15)–(3.17)). Otherwise we have to use interpolation, which affects noise. In our case the reconstruction grid is aligned with the direction of the primary beams (the y-axis), and all the nodes are located precisely at the midpoints between neighboring primary beams. Thus, no interpolation along the source direction is neeed. The only interpolation that is performed during reconstruction is along the detector direction. In the worst case, when all B_{ij} project precisely onto the detection points, noise level in the image is the highest and is given by (3.33). In the best case, when all B_{ij} project precisely onto the midpoints between the detection points, noise level in the image is the lowest and can be obtained by dividing the right-hand side of (3.33) by $\sqrt{2}$. In our experiments we assume that the standard deviation of noise $\hat{\sigma}_{j,k,l}$ is independent of k and l (cf. (3.17)), which justifies the factor $1/\sqrt{2}$. In practice, since we average $\sigma(B_{ij})$ over many points, the final value of $\bar{\sigma}$ should be somewhere between the two extremes.

In Figure 3.5 we show the noise estimates for different values of C_4 by vertical blue intervals. The top point for each interval is computed using (3.33) for all B_{ij} inside the disk of radius R_0 and averaging, and the bottom point is obtained by dividing the top one by $\sqrt{2}$. The red curve represents the observed noise levels $\bar{\sigma}$. As is seen, the experimentally observed curve is in good agreement with theoretical estimates. Formula (3.30) gives the optimal value $C_4^{\text{opt}} \approx 0.37$, which agrees well with the results in Figures 3.4 and 3.5. A reconstruction using the optimal set of C_j's is shown in Figure 3.6. Two cross-sections through the reconstructions with the optimal $C_4 = 0.37$ and non-optimal $C_4 = 1$ are shown in Figure 3.7.

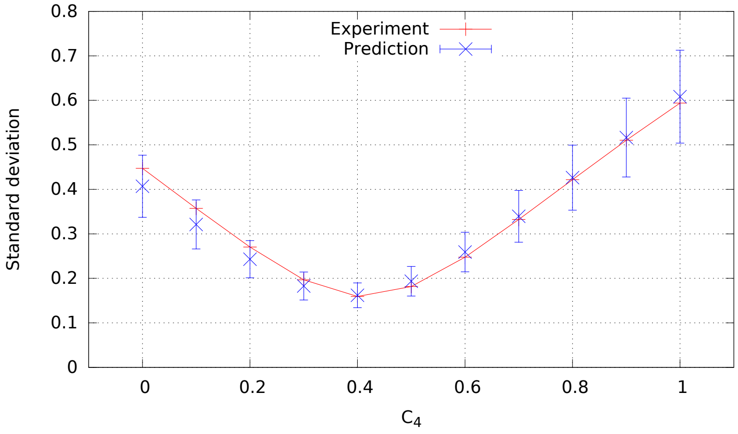

Figure 3.5: Theoretical and measured standard deviations $\sigma(C_4)$ and $\bar{\sigma}(C_4)$ in the reconstructed image in the case of four detectors and energy-independent attenuation.

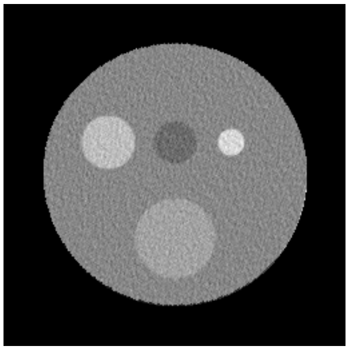

Figure 3.6: Optimal reconstruction in the case of four detectors. The attenuation coefficient μ is independent of energy.

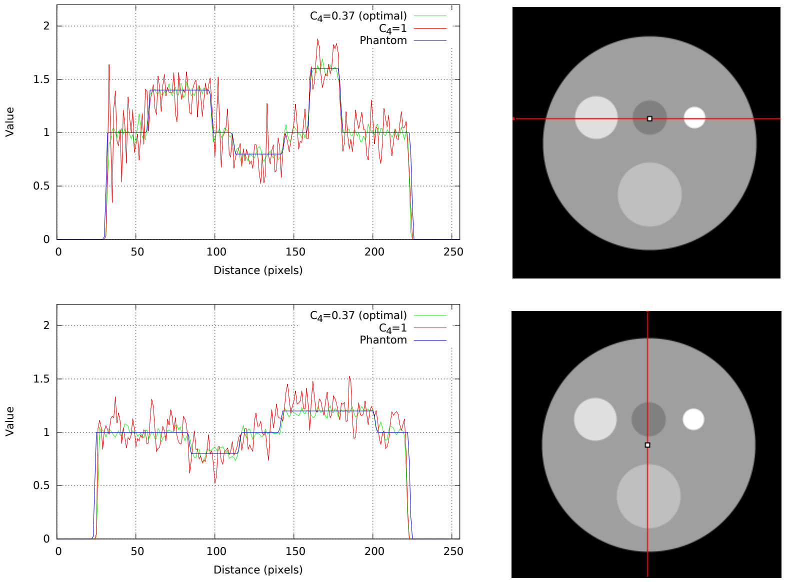

Figure 3.7: Cross-sections through the density plots of the attenuation coefficient along the lines shown on the right. The exact curve is blue, reconstruction with optimal parameters is shown in green, and reconstruction with non-optimal parameters – in red. The case of four detectors and energy-independent μ.

3.4.2 Exact inversion formula, energy-dependent μ.

As before, we assume that there are four detectors. In this case noise optimization is not possible and the coefficients $\{C_j\}$ and $\{B_j\}$ are obtained by solving (3.24). The data are simulated using (3.39).

In Figure 3.8 we show the reconstructions from noise-free data for the energies $E = 250$KeV, 490KeV, and 720KeV. The horizontal and vertical cross-sections through the three reconstruction of Figure 3.8 are shown in Figure 3.9.

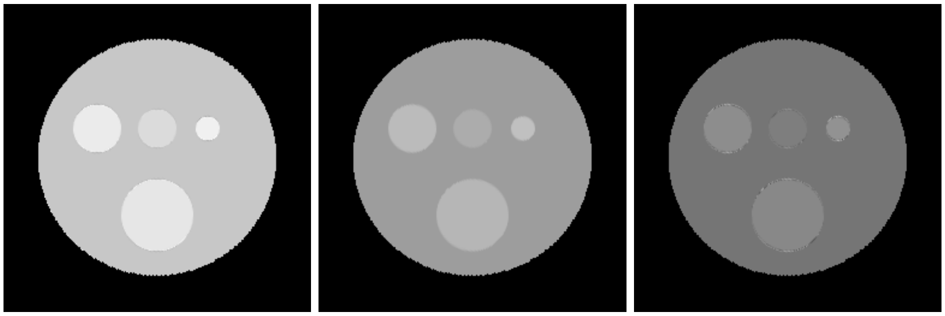

Figure 3.8: Reconstructions with the exact inversion formula (3.11) for a few energies in the range $[E_{\min}, E_{\max}]$, where $E_{\min} \approx 242\text{KeV}$ and $E_{\max} \approx 729\text{KeV}$, in the case of four detectors. Left to right: $E = 250$KeV, 490KeV, and 720KeV.

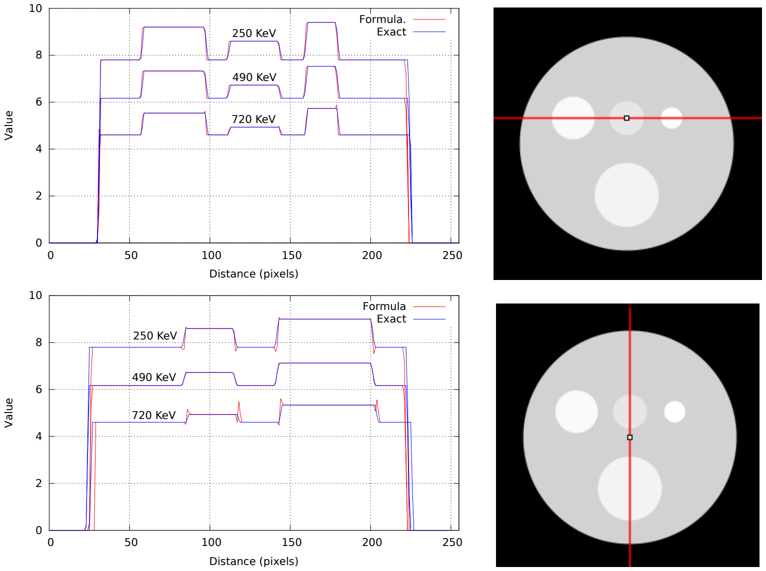

Figure 3.9: Cross-sections through the density plots of the reconstructions shown in Figure 3.8 along the lines shown on the right. The exact curves are blue, and the curves reconstructed using the inversion formula (3.11) – red. The case of four detectors.

3.4.3 Noise minimization in the case of energy-dependent attenuation.

To test the noise minimization technique described in Section 3.2.2 we suppose that there are five detectors. The data are simulated using (3.39) and contaminated by 0.1% noise.

To illustrate the reduction of noise provided by the approach in Section 3.2.2, we pick two energies $E_{1,2} \in [E_{\min}, E_{\max}]$, and compare two reconstructions for each of the energies. One reconstruction uses optimal coefficients described by (3.30). The other reconstruction uses non-optimal coefficients. Note that if the C_j's are known, the formula (3.14) allows us to compute $\mu(E_0)$ without using B_j's. Thus, for the non-optimal reconstruction of $\mu(E_1)$ we set $E_0 = E_1$ in (3.20)–(3.23), choose a non-optimal C_5, solve the rest of the equations for $C_1, \dots, C_4$, and then use formula (3.14). Reconstruction of $\mu(E_2)$ is done the same way.

We selected $E_1 = 400$KeV and $E_2 = 500$KeV. In the case of optimal reconstruction, μ is computed using the combination $C_j + \Delta E B_j$ as coefficients (cf. (3.14)). In the non-optimal case, we use only C_j's. Thus, to make the comparison of optimal and non-optimal coefficients meaningful, we list in Table 3.1 the values of $C_j + \Delta E B_j$ in the optimal case, and of C_j's – in the non-optimal case.

Table 3.1: Reconstruction coefficients in the inversion formula (3.14). The case of five detectors.

	Optimal ($C_j + \Delta E B_j$)	Non-optimal (C_j)
400 KeV	(-0.172, 0.698, -0.172, 0.322, 0.322)	(-1.049, 0.698, 0.706, -0.555, 1.20)
500 KeV	(0.323, -0.120, 0.323, 0.238, 0.238)	(-0.640, -0.120, 1.285, -0.725, 1.20)

The results of four reconstructions are shown in Figure 3.10. As expected, optimal parameters lead to a reduction in noise compared to non-optimal ones. Cross-sections through the reconstructions at $E_1 = 500$KeV are shown in Figure 3.11.

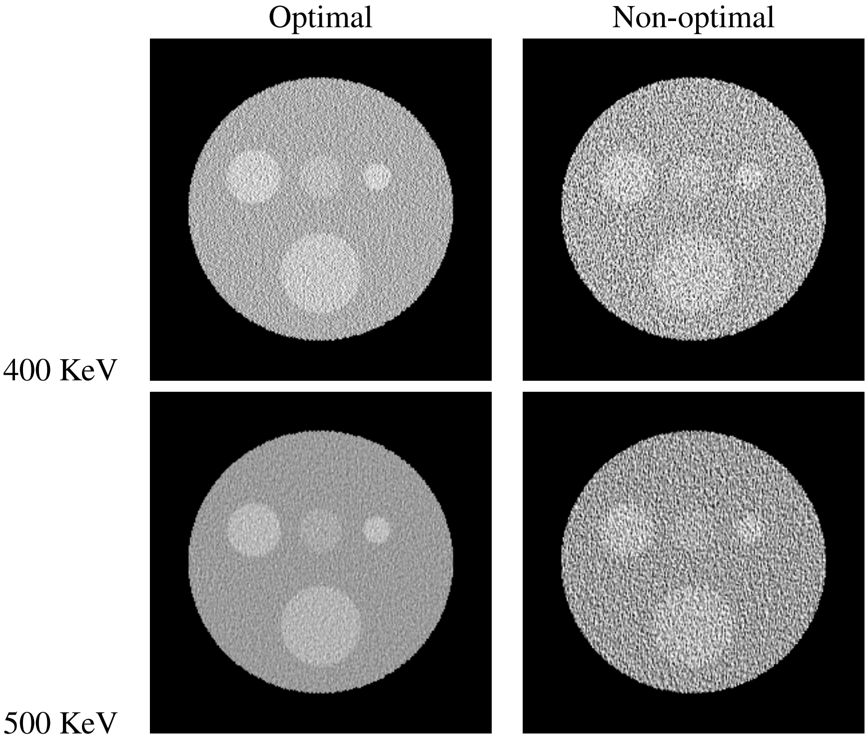

Figure 3.10: Reconstructions based on the inversion formula with optimal and non-optimal coefficients from five-detector data contaminated by 0.1% noise at 400 KeV(top) and 500 KeV(bottom).

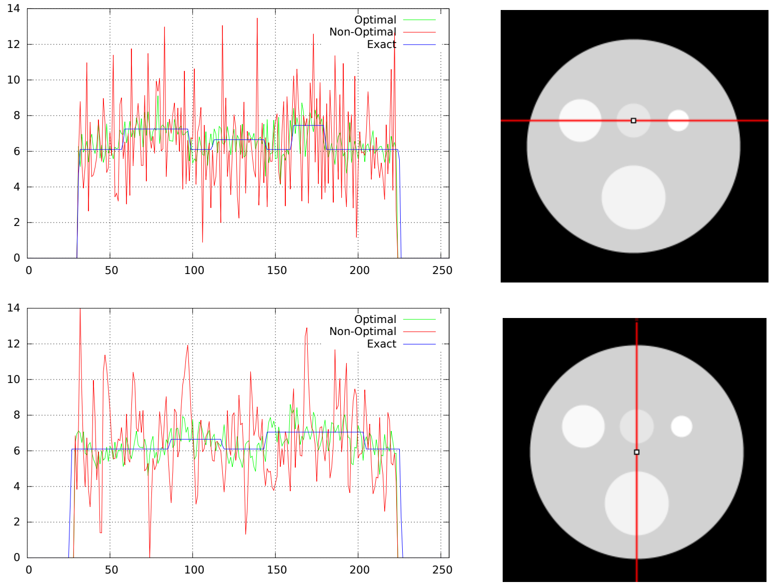

Figure 3.11: Cross-sections through the density plots of the reconstructions at 500 KeV of Figure 3.10 along the lines shown on the right. Exact curves are blue, reconstruction with optimal parameters – green, and non-optimal reconstruction – red. The case of five detectors.

The standard deviation of noise in the reconstructed image as a function of energy is shown in Figure 3.12. Theoretical estimates of the predicted standard deviation σ and observed values of $\bar{\sigma}$ are computed for several $E \in [E_{\min}, E_{\max}]$ using the approach of Section 3.4.1. Again, the observed curve and the prediction are in good agreement.

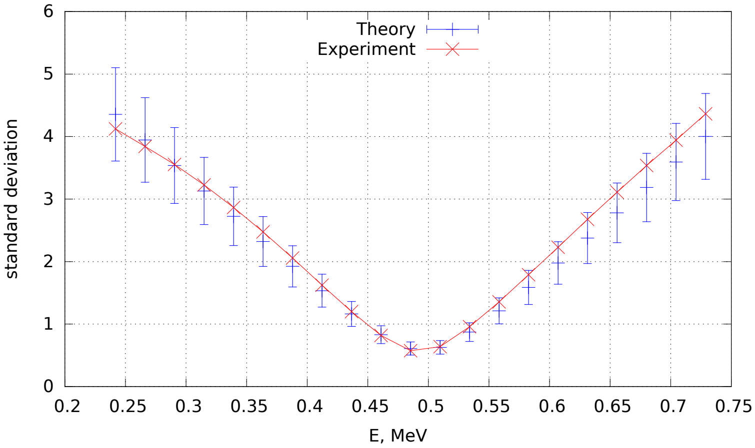

Figure 3.12: Theoretical (min/max σ) and measured ($\bar{\sigma}$) standard deviations of noise in the reconstructed image as functions of energy. The case of five detectors, the data are contaminated by 0.1% noise.

3.4.4 Iterative reconstruction

The first experiment in this subsection is with four detectors and energy-independent attenuation. Since the main advantage of iterative methods is improved noise stability, we consider reconstructions only from noisy data. In Figure 3.13 we see the effect of noise level in the data on image quality. One set of reconstructions is done with the iterative method of Section 3.3.1. The other set is done using the inversion formula (3.35).

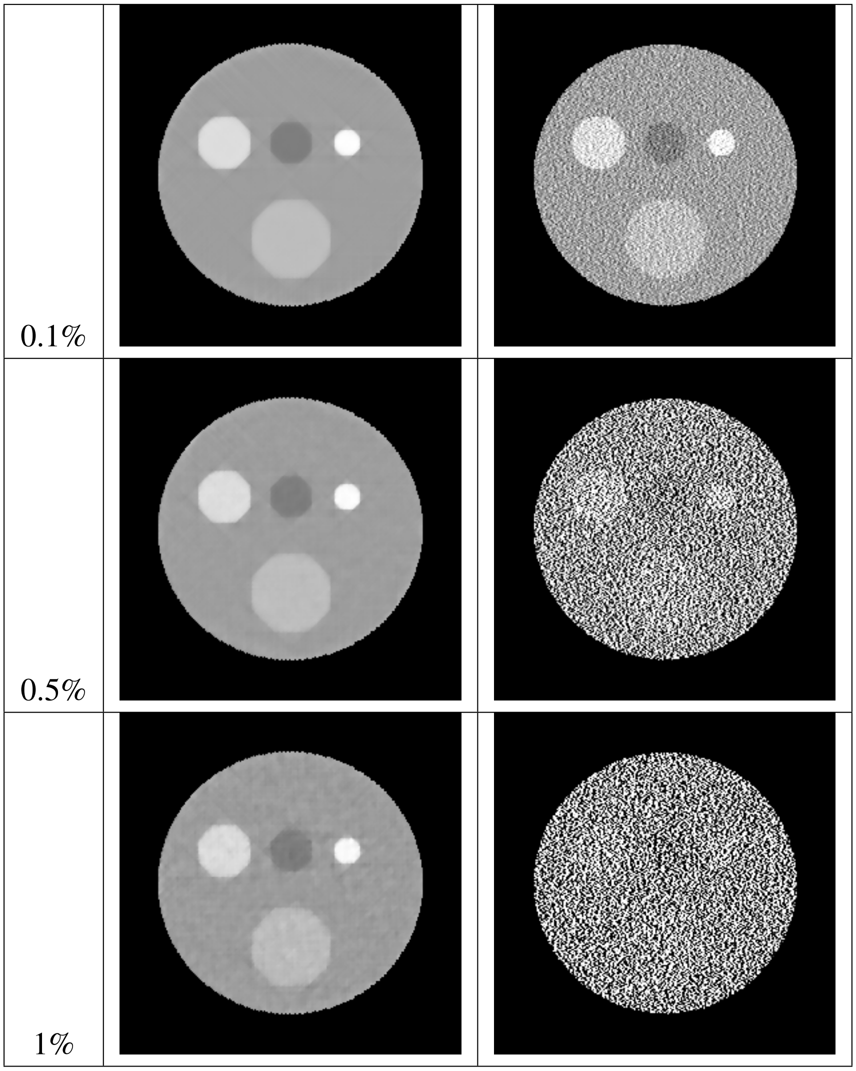

Figure 3.13: Reconstructions from four-detector data contaminated by noise of various levels, energy-independent attenuation. Left - iterative algorithm, right - inversion formula (3.11) with optimal $C_j, j = 1, \ldots, 4$ (cf. (3.34)).

Note that the reconstruction grid step-sizes in both directions are equal to 1, so the projection matrices $P^{(1)}$ and $P^{(2)}$ have entries of approximately the same magnitude. Therefore, in (3.37) we chose for simplicity $\lambda_u = \lambda_v =: \lambda$. Then, for reconstruction presented below, we use an optimal value of λ: $\lambda = 1$ for noise levels 0.1% and 0.5%, and $\lambda = 2$ – for noise level 1%. These values are found experimentally by minimizing $\|\mu(B;\lambda) - \mu_{\text{true}}(B)\|$ for each noise level. Here $\mu(B;\lambda)$

is the result of iterative reconstruction for the given λ, and $\mu_{\text{true}}(B)$ is the correct distribution of the attenuation coefficient shown in Figure 3.3. In practice such optimization is never possible, but it is useful anyway since it allows investigation of the dependence of regularization parameters on noise level. Besides, our experiments showed that the results of reconstructions are not too sensitive to changes in λ.

The results of local iterative reconstruction from four detector data contaminated by different levels of noise in the case of energy-independent attenuation are shown in Figure 3.14. The radius of the ROI equals 50. We use the algorithm in Section 3.3.2. First we find the weights that equalize the magnitudes of all the unknowns, and then use the same regularization weight λ in front of all the TV terms. We use the same values of λ as in the case of global reconstruction described above.

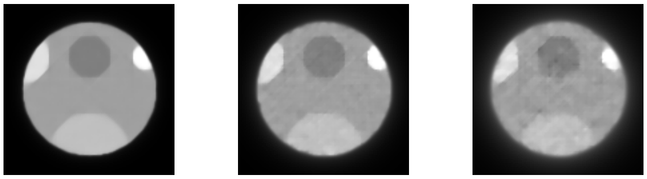

Figure 3.14: Local iterative reconstruction from four detector noisy data in the case of energy-independent attenuation. Left to right: 0.1% noise, 0.5% noise, 1% noise.

Finally, the performance of the algorithm based on (3.40) in the case of five detectors and energy-dependent attenuation is illustrated by the results in Figure 3.15. As before, we first find the weights that equalize the magnitudes of all the unknowns, and then use the same regularization weight λ in front of all the TV terms. We use the same values of λ for each noise level as in the energy-independent case. The reconstructed μ at three energies $E = 250\text{KeV}$, $E = 490\text{KeV}$, and $E = 720\text{KeV}$ are shown in Figures 3.15 and 3.16.

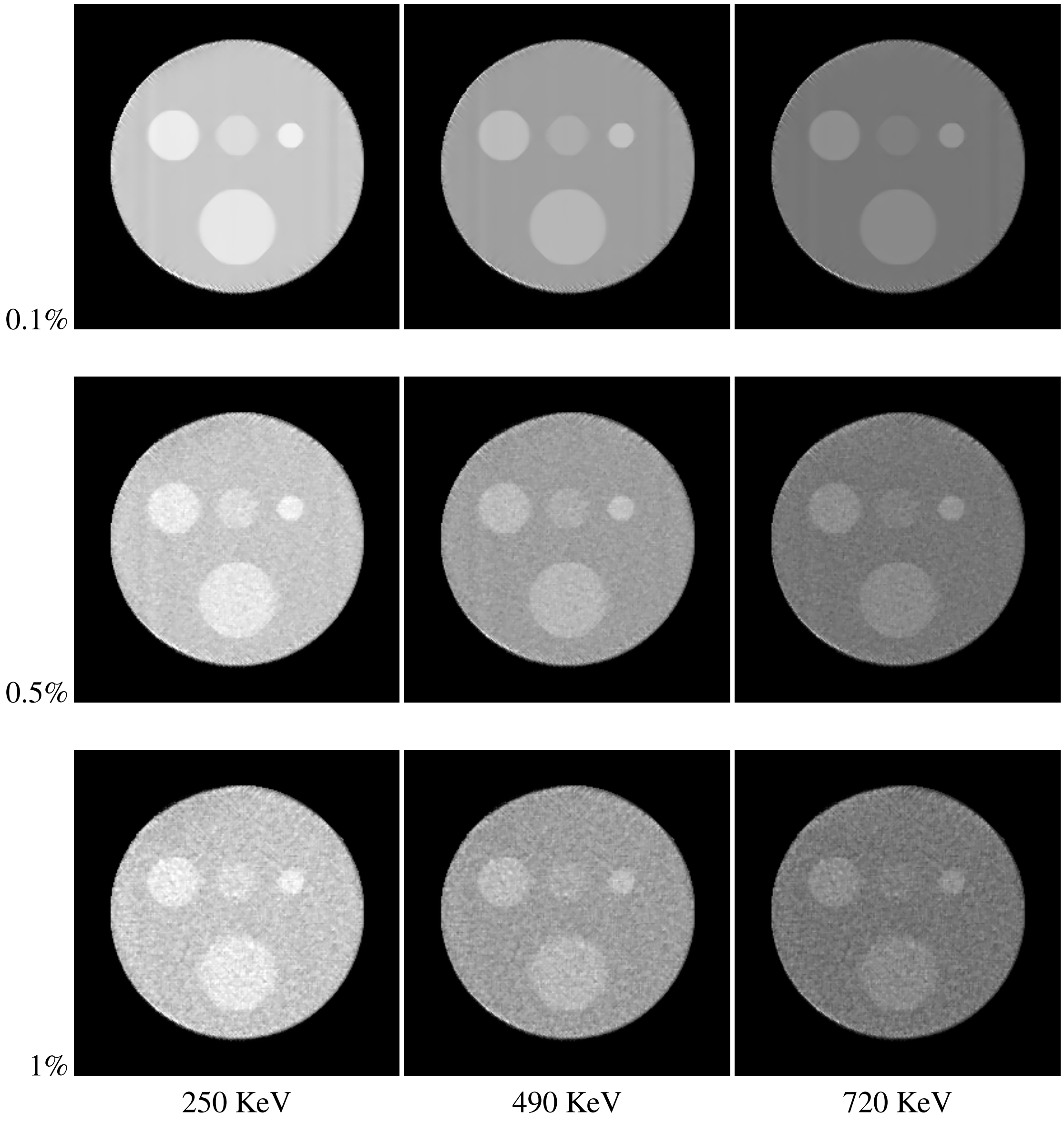

Figure 3.15: Iterative reconstruction from five-detector data contaminated by different levels of noise. Energy-dependent μ.

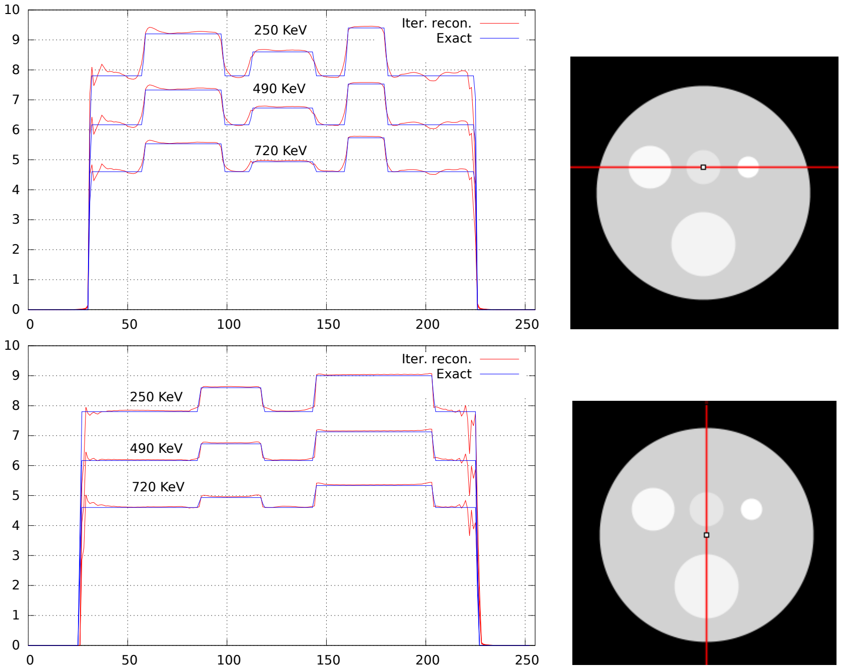

Figure 3.16: Cross-sections through the density plots of the reconstructions of Figure 3.15 corresponding to 0.1% noise along the lines shown on the right. Exact μ – blue, reconstructed μ – red.

CHAPTER 4: CONCLUSION

We derived a local inversion formula (3.11) of BRT for the case with four or more detectors that allows noise minimization in the reconstruction. The inversion formula involves only the first derivative of the measured data which leads to a simple and stable numerical reconstruction algorithm. In the case when the noise minimization is not necessary, the inversion formula requires only three detectors.

We generalized the exact inversion formula to accommodate Compton energy shifts for the case of four or more detectors. To take multiple scattering energies into account we used linear approximation to the dependence of the attenuation on energy. We developed an algorithm for noise minimization in the reconstruction which requires five or more detectors for the case when the attenuation depends on energy.

We developed an iterative reconstruction algorithm that has higher noise stability, can solve an interior problem and works in the case of energy-dependent attenuation.

We note that all the algorithms developed in this work can be generalized to curved detectors with a fixed focus. Indeed, our key starting point is differentiation of the equation (3.6) along the direction β_j to obtain (3.7). The same step can be made when $\mathcal{D}_j$ is focused at a single point, because the angle between the primary beam AB and scattered beam BD_j remains constant when applying ∇_j. This, however, no longer holds for fan beam geometry. In this case the source is fixed, the angle between AB and BD_j is not constant, and application of ∇_j to (3.6) leads to the appearance of additional terms not present in (3.7).

The numerical experiments presented in this work are by no means exhaustive, and are designed only as a proof-of-principle study. This is why we use one of the simplest optimization methods and do not discuss many practical issues like computational complexity, number of iterations, etc. In the future, faster convergent algorithms based e.g. on Nesterov acceleration or conjugate gradients can be used, and more detailed experiments should be performed.

APPENDIX : SYMMETRY PROPERTIES OF COEFFICIENTS c_{ij}

Using (2.56) we obtain that the differential operator in brackets on the right of (2.57) is given by

$$[\cdot] = -(l_1(c_{13}^\perp + c_{21}^\perp)\nabla_1^\perp + l_2(c_{21}^\perp + c_{32}^\perp)\nabla_2^\perp + l_3(c_{13}^\perp + c_{32}^\perp)\nabla_3^\perp). \tag{A.1}$$

Then we write $g_{12} = g_1 - g_2$, $g_{32} = g_3 - g_2$, and expand the differential operators acting on g_2 with respect to ∇_2 and $\nabla_2^\perp$ (cf. (2.5)). In (2.58) there are no terms containing $\nabla_2^\perp g_2$, hence they must cancel. Since l_1, l_2 and l_3 are independent of each other, we should show that all the terms containing $l_i\nabla_2^\perp g_2$ cancel for $i = 1, 2, 3$. Consider, for example, the coefficient in front of $l_1\nabla_2^\perp$. Using (2.55) and (A.1) we compute that this coefficient is indeed zero:

$$\begin{aligned}&(c_{12} - c_{13})(c_{13}^\perp + c_{21}^\perp)(-c_{21}^\perp) + (1 - c_{12})(c_{13}^\perp + c_{21}^\perp)c_{32}^\perp + (c_{13}^\perp + c_{21}^\perp)\Sigma c_{12}\\ &= (c_{13}^\perp + c_{21}^\perp)[c_{13}c_{21}^\perp + c_{32}^\perp + c_{12}c_{13}^\perp] = (c_{13}^\perp + c_{21}^\perp)[c_{32}^\perp - c_{32}^\perp] = 0.\end{aligned} \tag{A.2}$$

The other two coefficients can be handled in a similar fashion. To establish (2.59) we have to compute the coefficients in front of $l_i\nabla_2$, $i = 1, 2, 3$. Consider, for example, the case $i = 1$.

$$\begin{aligned}&-(c_{12} - c_{13})(c_{13}^\perp + c_{21}^\perp)c_{12} - (1 - c_{12})(c_{13}^\perp + c_{21}^\perp)c_{23} - (c_{13}^\perp + c_{21}^\perp)\Sigma c_{21}^\perp\\ &= -(c_{13}^\perp + c_{21}^\perp)[1 + c_{23} - c_{13}c_{12} + c_{21}^\perp c_{13}^\perp - c_{12}c_{23} + c_{21}^\perp c_{32}^\perp]\\ &= -(c_{13}^\perp + c_{21}^\perp)[1 + c_{23} - c_{23} - c_{13}] = (c_{13}^\perp + c_{21}^\perp)[c_{13} - 1],\end{aligned} \tag{A.3}$$

which coincides with the appropriate term in (2.59). The other terms can be evaluated in a similar fashion.

LIST OF REFERENCES

[Amb12] G. Ambartsoumian, *Inversion of the V-line Radon transform in a disc and its applications in imaging*, Computers and Mathematics with Applications **64** (2012), 260–265.

[Bra83] Libby Frances Brateman, *Compton scatter axial tomography with x-rays*, Ph.D. thesis, University of Florida, 1983.

[Bus02] Jerrold T. Bushberg, *The essential physics of medical imaging*, Lippincott Williams & Wilkins, 2002.

[BZG97] R. Basko, G. L. Zeng, and G. T. Gullberg, *Analytical reconstruction formula for one-dimensional Compton camera*, IEEE Transactions on Nuclear Science **44** (1997), 1342–1346.

[CD73] R.L. Clarke and G. Van Dyk, *A new method for measurement of bone mineral content using both transmitted and scattered beams of gamma-rays*, Phys. Med. Biol. **18** (1973).

[CW11] W. Cong and G. Wang, *X-ray scattering tomography for biological applications*, Journal of X-Ray Science and Technology **19** (2011), 219–227.

[FMS11] L. Florescu, V. Markel, and J. C. Schotland, *Inversion formulas for the broken-ray Radon transform*, Inverse Problems **27** (2011), article ID: 025002 (13pp).

[FSM09] L. Florescu, J. C. Schotland, and V. Markel, *Single scattering optical tomography*, Physical Review E **79** (2009), article ID: 036607 (13pp).

[Get12] P. Getreuer, *Rudin-Osher-Fatemi Total Variation Denoising using Split Bregman*, Image Processing On Line (2012), http://dx.doi.org/10.5201/ipol.2012.g-tvd.

[GKKW73] E. S. Garnett, T.J. Kennet, D. B. Kenyon, and C. E. Webber, *A photon scattering technique for the measurement of absolute bone density in man*, Radiology **106** (1973).

[HK87] G. Harding and J. Kosanetzky, *Status and outlook of coherent-x-ray scatter imaging*, Journal of Optical Society of America **4** (1987).

[KK13] A. Katsevich and R. Krylov, *Broken ray transform: inversion and a range condition*, Inverse Problems **29** (2013), article ID 075008 (15 pp).

[MNTZ10] M. Morvidone, M. K. Nguyen, T. T. Truong, and H. Zaidi, *On the V-line Radon transform and its imaging applications*, International Journal of Biomedical Imaging **2010** (2010), article ID: 208179 (6 pp).

[Nat01] F. Natterer, *The Mathematics of Computerized Tomography*, Classics in Applied Mathematics 32, SIAM, Philadelphia, 2001.

[Pod10] E. B. Podgoršak, *Radiation Physics for Medical Physicists*, second ed., Springer, Heidelberg, 2010.

[TN11] T. T. Truong and M. K. Nguyen, *On new V-line Radon transforms in* $\mathbb{R}^2$ *and their inversion*, Journal of Physics A: Mathematical and Theoretical **44** (2011), article ID: 075206 (13pp).

[ZSM14] F. Zhao, J. C. Schotland, and V. A. Markel, *Inversion of the star transform*, Inverse Problems **30** (2014), article ID: 105001 (31pp).